Computational electro- and magneto-elasticity for quasi-incompressible media immersed in free space

Jean-Paul Pelteret[1,*], Denis Davydov[1], Andrew McBride[2], Duc Khoi Vu[1] and Paul Steinmann[1]

[1]*Chair of Applied Mechanics, University of Erlangen–Nuremberg, Paul-Gordan Straße 3, Erlangen 91052, Germany*
[2]*Infrastructure and Environment, School of Engineering, University of Glasgow, Glasgow G12 8QQ, United Kingdom*

SUMMARY

In this work a mixed variational formulation to simulate quasi-incompressible electro- or magneto-active polymers immersed in the surrounding free space is presented. A novel domain decomposition is used to disconnect the primary coupled problem and the arbitrary free space mesh update problem. Exploiting this decomposition we describe a block iterative approach to solving the linearised multiphysics problem, and a physically and geometrically based, three-parameter method to update the free space mesh. Several application-driven example problems are implemented to demonstrate the robustness of the mixed formulation for both electro-elastic and magneto-elastic problems involving both finite deformations and quasi-incompressible media. Copyright © 2016 John Wiley & Sons, Ltd.

Received ...

KEY WORDS: Nonlinear electro-/magneto-elasticity; quasi-incompressible media; free space; finite strain

*Correspondence to: Jean-Paul Pelteret, Chair of Applied Mechanics, University of Erlangen–Nuremberg, Paul-Gordan Straße 3, Erlangen 91052, Germany. E-mail: jppelteret.fau@gmail.com

Contract/grant sponsor: European Research Council (ERC) Advanced Grant MOCOPOLY; contract/grant number: 289049

1. INTRODUCTION

The interaction between elastic bodies and electromagnetic fields has been a subject of study for many decades. Field-responsive polymers are an interesting class of smart materials that deform and alter their material characteristics under the influence of electric or magnetic fields. These electro-active polymers (EAPs) and magneto-active polymers (MAPs) have recently found application in, for example, general engineering as actuators, valves and damping devices [1, 2, 3] and the biomedical field as artificial muscles [4, 5]. However, the numerical modelling of EAPs and MAPs still poses serious challenges that need to be addressed in both the understanding and simulation of field-sensitive bodies under the influence of an electric or magnetic field.

Much work is being done to characterise these materials in order to further enhance their properties. Due to their polymer nature, both EAPs and MAPs often exhibit both incompressible and viscoelastic behaviour. In dielectric actuators, instabilities are often exhibited at the high electric fields needed to obtain large deformations (driven by Coulombic forces) [6, 7]. Fundamentally different behaviour is demonstrated by MAPs, with either magnetostriction or magneto-elongation developing depending on the arrangement of their microstructure [8, 9, 10, 11, 12]. Analysis of the constitutive response of such materials [13, 14, 15, 16, 17, 18] typically assumes that the body is incompressible.

Numerous examples of finite-strain coupled numerical models of EAPs [19, 20, 21, 22, 23, 24, 25] and MAPs [26, 27, 18] can be found in the literature. In the context of electro-elastic problems, mixed variational principals have been used by Ortigosa and Gil [28], Rodríguez-Ramos et al. [29], Yang and Batra [30], and Zwecker et al. [21]. We note that in all the aforementioned works for EAPs, only their material bodies were considered and discretised using the finite element method, which is a reasonable approach for simulating condensator-like structures whose thickness is very small in comparison with other dimensions. However, unlike the simulation of piezoelectric materials [31] under electric stimulation for which the electric field in the free space surrounding a material body can be in many cases ignored because of its minor importance, in dealing with EAPs the contribution of the free space can, in some cases, become significant and must be taken into account [32, 33]. This is mainly due to the fact that the electric permittivity of most EAPs is considerably weak; for many EAPs it is of approximately one order greater magnitude than that of a vacuum [34]. Similarly, it is well understood that forces arising from the Maxwell stress [35, 36] in the free space are often central to functioning of MAP-based devices, and therefore should be accounted for within macroscopically-focussed numerical models [26, 18]. In some cases, due to stability issues arising from its inclusion, the Maxwell stress contribution is ignored [37].

When the contribution of the free space is important, one of two approaches is typically used. In the first approach (FEM with truncation of free space), the finite element method is employed with a finite element mesh that extends considerably beyond the body in order to capture the correct response of the system (the deformable body and surrounding free space). In the second approach the finite element method is used in combination with the boundary element method (coupled BEM-FEM [38, 39, 40]). Despite the fact that coupled BEM-FEM is relatively easy to implement, work still needs to be done to improve the numerical efficiency of the simulation process since the resulting system of equations is dense and non-symmetric. In this respect, at the current state of development, the FEM with truncation of free space is a reasonable choice. The implementation

of this approach is, however, not straightforward. The Maxwell stress must be accounted for in a practical manner and a robust scheme for describing the movement of the free space mesh during large deformations of the elastic body must be provided. Furthermore, the use of a traditional, monolithic mesh update scheme would introduce a large number of additional degrees-of-freedom to the global system and destroy its symmetry due to one-way coupling at the solid-free space interface.

In this work, we present a general implementation of the quasi-incompressible coupled finite element problem with truncation of free space. From a total energy functional we derive in full the variational formulation of the mixed problem, along with its first and second variation, and the resulting finite element discretisation. A novel domain decomposition is used in conjunction with a staggered mesh update scheme, thereby leading to a smaller and symmetric primary system of equations to solve. A general, physically-based mesh update algorithm that is easy to implement, tuned to the problem geometry, and sufficiently robust for finite deformations is presented. Decoupling the primary and mesh-motion problems also allows for the development of focussed iterative solving strategies for the linearised multi-physics problem, two of which are shown here. The use of these methods are illustrated using examples derived from practical problems involving finite deformation of highly incompressible media. As it consolidates and details the key concepts required to implement problems involving EAPs and MAPs, this paper also aims to serve as a starting point for future development in this field of research.

The remainder of this manuscript is composed as follows: In section 2 a brief review of nonlinear electro-/magneto-statics and electro-/magneto-elastostatics is presented. Some points regarding constitutive modelling are discussed in section 3. The variational formulation is then presented in section 4, after which details of the finite element discretisation are provided in section 5. Two methods of solving the linearised problem using a block-iterative approach is given in section 6. Section 7 is dedicated to describing a secondary problem following from the truncation of free space. Finally, illustrative numerical examples are presented in section 8, followed by a discussion and conclusion.

2. KINEMATICS AND BALANCE LAWS

We consider the general case of a deformable solid immersed in free space with the closure of the material configuration (that of zero strain and stress) denoted by $\overline{\mathcal{B}_0} = \mathcal{B}_0 \cup \partial\mathcal{B}_0$ surrounded by free space $\overline{\mathcal{S}_0}$. Application of a load results in the reference state of the body, depicted in figure 1, deforming to $\overline{\mathcal{B}_t}$ and the free space to $\overline{\mathcal{S}_t}$. The extents of the truncated domain, namely the far-field boundary, remains fixed in shape (topologically constant), namely $\partial\mathcal{S}_0 = \partial\mathcal{S}_t$. We define a nonlinear deformation function $\mathbf{x} = \boldsymbol{\varphi}(\mathbf{X})$ that maps points $\mathbf{X} \in \overline{\mathcal{B}_0 \cup \mathcal{S}_0}$ to $\mathbf{x} \in \overline{\mathcal{B}_t \cup \mathcal{S}_t}$. We assume that $\partial\mathcal{B}_0$ and $\partial\mathcal{S}_0$ admit the decomposition $\partial\mathcal{B}_0 = \overline{\partial\mathcal{B}_0^{\boldsymbol{\varphi}} \cup \partial\mathcal{B}_0^{\mathbf{t}}} = \overline{\partial\mathcal{B}_0^{\Phi} \cup \partial\mathcal{B}_0^{\mathbb{D}}}$ and $\partial\mathcal{S}_0 = \overline{\partial\mathcal{S}_0^{\Phi} \cup \partial\mathcal{S}_0^{\mathbb{B}}}$, where $\partial\mathcal{B}_0^{\boldsymbol{\varphi}} \cap \partial\mathcal{B}_0^{\mathbf{t}} = \emptyset$, $\partial\mathcal{B}_0^{\Phi} \cap \partial\mathcal{B}_0^{\mathbb{D}} = \emptyset$ and $\partial\mathcal{S}_0^{\Phi} \cap \partial\mathcal{S}_0^{\mathbb{B}} = \emptyset$. Here $\partial\mathcal{B}_0^{\boldsymbol{\varphi}}$ and $\partial\mathcal{B}_0^{\mathbf{t}}$ respectively denote the portions of $\partial\mathcal{B}_0$ with either prescribed deformation or traction. Similarly, the areas of $\partial\mathcal{B}_0$ with prescribed electric potential and electric flux are respectively denoted as $\partial\mathcal{B}_0^{\Phi}$ and $\partial\mathcal{B}_0^{\mathbb{D}}$. The portion of the truncated far field boundary with either a prescribed magnetic scalar potential or magnetic flux are given by $\partial\mathcal{S}_0^{\Phi}$ and $\partial\mathcal{S}_0^{\mathbb{B}}$, respectively.

We define two differential operators; ∇_0 being that with respect to $\mathbf{X}$ and ∇ with respect to $\mathbf{x}$. The deformation gradient is given by $\mathbf{F} = \nabla_0 \mathbf{x}$, and it is necessary that its determinant $J = \det \mathbf{F} > 0$ to ensure that $\boldsymbol{\varphi}$ remains a one-to-one map that prevents self-penetration of the material.

In this work we will consider two distinct cases, namely that of the material being responsive to electric fields alone, and the other being when the media is sensitive to only magnetic fields. As will be shown below, there exist numerous similarities in the equations governing these scenarios. Therefore it is relatively simple to implement these equations in a general way such that either case can be considered independently.

In the absence of free charges, the governing equations for electro-statics as given by Faraday's law of induction and Gauss's law [41, 42] in terms of referential quantities are

$$\nabla_0 \times \underline{\mathbb{E}} = \mathbf{0} \quad , \quad \nabla_0 \cdot \underline{\mathbb{D}} = 0 \quad \text{in} \quad \mathcal{B}_0 \cup \mathcal{S}_0 \quad . \tag{1}$$

Here $\underline{\mathbb{E}}$ and $\underline{\mathbb{D}}$ respectively denote the electric field and displacement (sometimes called the electric induction) vectors, as defined in the material configuration. Alternatively, assuming that the material is electrically non-conductive and that there exist no free currents, then the static form of Maxwell's equations are defined by Ampére's law and Gauss's law dictating that no magnetic monopoles are present [43, 41, 44, 18], that is

$$\nabla_0 \times \underline{\mathbb{H}} = \mathbf{0} \quad , \quad \nabla_0 \cdot \underline{\mathbb{B}} = 0 \quad \text{in} \quad \mathcal{B}_0 \cup \mathcal{S}_0 \quad . \tag{2}$$

The referential magnetic field and induction vectors are given by $\underline{\mathbb{H}}$ and $\underline{\mathbb{B}}$ respectively. The continuity conditions on $\partial\mathcal{B}_0$ are given by either of

$$\begin{aligned} [\![\underline{\mathbb{E}}]\!] \times \mathbf{N} = \mathbf{0} \quad , \quad [\![\underline{\mathbb{D}}]\!] \cdot \mathbf{N} = 0 \\ [\![\underline{\mathbb{H}}]\!] \times \mathbf{N} = \mathbf{0} \quad , \quad [\![\underline{\mathbb{B}}]\!] \cdot \mathbf{N} = 0 \end{aligned} \quad \text{on} \quad \partial\mathcal{B}_0 \tag{3}$$

which enforce that the tangential component of the electric and magnetic fields, as well as the normal component of the electric and magnetic induction, remain continuous on the boundary $\partial\mathcal{B}_0$ with outward normal $\mathbf{N}$. Here we define the jump as $[\![\bullet]\!] \coloneqq [\bullet]^+ - [\bullet]^-$, where $[\bullet]^+$ and $[\bullet]^-$ respectively denote the one-sided limit of the function $(\bullet)$ from the outward and inward normal directions. Note that when body and surface charges are to be considered, suitable amendments to equation $(1)_2$ and equation $(3)_2$ (namely those discussed by [45]) have to be made. Similarly, for the case when body and surface free currents must be accounted for, equation $(2)_1$ and equation $(3)_3$ require modification [46].

The fundamental constitutive equations that link the various electric and magnetic quantities are [41, 47, 48, 49]

$$\begin{aligned} \underline{\mathbb{D}} &= \varepsilon_0 J \mathbf{C}^{-1} \cdot \underline{\mathbb{E}} + \underline{\mathbb{P}} \quad , \\ J^{-1} \mathbf{C} \cdot \underline{\mathbb{B}} &= \mu_0 \left[\underline{\mathbb{H}} + \underline{\mathbb{M}} \right] \end{aligned} \tag{4}$$

where $\mathbf{C} = \mathbf{F}^T \cdot \mathbf{F}$ is the right Cauchy–Green deformation tensor, the free space electric permittivity constant $\varepsilon_0 = 8.854 \times 10^{-12}\,\mathrm{F\,m^{-1}}$ and the free space magnetic permeability constant $\mu_0 =$

$4\pi \times 10^{-7}\mathrm{H\,m}^{-1}$. The two additional material quantities $\underline{\mathbb{P}}$ and $\underline{\mathbb{M}}$ describe the polarisation and magnetisation in the solid media (and therefore vanish in the free space).

For the elastic problem, the kinematic compatibility condition is

$$\nabla_0 \times \mathbf{F} = \mathbf{0} \quad \text{in} \quad \mathcal{B}_0 \quad . \tag{5}$$

In the case of fully incompressible media, the point-wise volumetric Jacobian J is unity. For both electro- or magneto-elastostatics, the Lagrangian form for the balance of linear momentum is expressed as [50, 51, 52, 41, 53, 49]

$$\nabla_0 \cdot \mathbf{P}^{\text{elas}} + \mathbf{b}_0^{\text{pon}} + \mathbf{b}_0 = \nabla_0 \cdot \mathbf{P}^{\text{tot}} + \mathbf{b}_0 = \mathbf{0} \quad \text{in} \quad \mathcal{B}_0 \cup \mathcal{S}_0 \quad , \tag{6}$$

where $\mathbf{P}$ denotes a Piola stress, along with the associated angular momentum balance equation [54, 55]

$$\mathbf{P}^{\text{tot}} \cdot \mathbf{F}^T = \mathbf{F} \cdot \left[\mathbf{P}^{\text{tot}}\right]^T \tag{7}$$

that ensures that the total Cauchy stress $\boldsymbol{\sigma}^{\text{tot}} = J^{-1}\mathbf{P}^{\text{tot}} \cdot \mathbf{F}^T = J^{-1}\mathbf{F} \cdot \mathbf{S}^{\text{tot}} \cdot \mathbf{F}^T$ (where $\mathbf{S}^{\text{tot}}$ is the total Piola–Kirchhoff stress tensor) is symmetric. The ponderomotive body force, as described by Pao [35], can be expressed as the divergence of a stress tensor

$$\mathbf{b}_0^{\text{pon}} = \nabla_0 \cdot \mathbf{P}^{\text{pon}} \equiv J^{-1}\mathbf{b}_t^{\text{pon}} = J^{-1}\nabla \cdot \boldsymbol{\sigma}^{\text{pon}} \tag{8}$$

and in the spatial setting has the compact expansion [48, 36]

$$\begin{aligned} \mathbf{b}_t^{\text{pon}} &= [\nabla \underline{\mathbb{e}}] \cdot \underline{\mathbb{p}} \quad \text{where} \quad \underline{\mathbb{e}} = \mathbf{F}^{-T} \cdot \underline{\mathbb{E}} \quad , \quad \underline{\mathbb{p}} = J^{-1}\mathbf{F} \cdot \underline{\mathbb{P}} \\ \mathbf{b}_t^{\text{pon}} &= \underline{\mathbb{m}} \cdot [\nabla \underline{\mathbb{b}}] \quad \text{where} \quad \underline{\mathbb{b}} = J^{-1}\mathbf{F} \cdot \underline{\mathbb{B}} \quad , \quad \underline{\mathbb{m}} = \mathbf{F}^{-T} \cdot \underline{\mathbb{M}} \end{aligned} \tag{9}$$

for the respective electric and magnetic cases. It describes the force exerted on the solid body due to the presence of an electric or magnetic field and, due to the electric or magnetic couple, prescribes that the elastic Cauchy stress $\boldsymbol{\sigma}^{\text{elas}}$ is not symmetric. We define the total stress as

$$\mathbf{P}^{\text{tot}} = \mathbf{P}^{\text{elas}} + \mathbf{P}^{\text{pon}} = \mathbf{P}^{\text{elas}} + \mathbf{P}^{\text{pol/mag}} + \mathbf{P}^{\text{max}} \tag{10}$$

where the ponderomotive stress is decomposed into a symmetric Maxwell stress tensor and a secondary component directly resulting from the polarisation or magnetisation of the solid material. For detailed discussions on the full expression of $\mathbf{P}^{\text{pon}}$, we refer the reader to [14, 16, 53, 36, 48, 56] and the references therein. Noting that $\mathbf{P} = J\boldsymbol{\sigma} \cdot \mathbf{F}^{-T}$, for the electric problem [48, 42]

$$\boldsymbol{\sigma}^{\text{pon}} = \underline{\mathbb{e}} \otimes \underline{\mathbb{d}} - \frac{1}{2}\varepsilon_0 \left[\underline{\mathbb{e}} \cdot \underline{\mathbb{e}}\right] \mathbf{i} \quad , \quad \boldsymbol{\sigma}^{\text{pol}} = \underline{\mathbb{e}} \otimes \underline{\mathbb{p}} \quad , \quad \boldsymbol{\sigma}^{\text{max}} = \varepsilon_0 \left[\underline{\mathbb{e}} \otimes \underline{\mathbb{e}} - \frac{1}{2}\left[\underline{\mathbb{e}} \cdot \underline{\mathbb{e}}\right] \mathbf{i}\right] \quad , \tag{11}$$

where $\mathbf{i}$ is the spatial identity tensor, while for the magnetic problem [35, 56]

$$\begin{gathered}\boldsymbol{\sigma}^{\text{pon}} = \frac{1}{2\mu_0}\left[\underline{\mathbb{b}}\cdot\underline{\mathbb{b}}\right]\mathbf{i} - \left[\underline{\mathbb{h}}\cdot\underline{\mathbb{b}}\right]\mathbf{i} + \underline{\mathbb{h}}\otimes\underline{\mathbb{b}} \quad , \quad \boldsymbol{\sigma}^{\text{mag}} = \mu_0\left[\frac{1}{2}\left[\underline{\mathbb{m}}\cdot\underline{\mathbb{m}}\right]\mathbf{i} + \underline{\mathbb{h}}\otimes\underline{\mathbb{m}}\right] \quad , \\ \boldsymbol{\sigma}^{\text{max}} = \mu_0\left[\underline{\mathbb{h}}\otimes\underline{\mathbb{h}} - \frac{1}{2}\left[\underline{\mathbb{h}}\cdot\underline{\mathbb{h}}\right]\mathbf{i}\right] \quad .\end{gathered} \tag{12}$$

It is also required that the mechanical traction applied at $\partial\mathcal{B}_0$ is balanced by the traction across a material interface

$$[\![\mathbf{P}^{\text{tot}}]\!]\cdot\mathbf{N} = \mathbf{t}_0 \quad \text{on} \quad \partial\mathcal{B}_0^{\mathbf{t}} \quad . \tag{13}$$

For the magnetic problem, as only quasi-static conditions are considered and the lack of free currents, we define a scalar potential [43, 41, 26] related to the curl-free magnetic field by

$$\underline{\mathbb{H}} \coloneqq -\nabla_0\Phi \quad \text{in} \quad \mathcal{B}_0\cup\mathcal{S}_0 \quad . \tag{14}$$

Although this quantity is convenient but fictitious for the magnetic problem, in the electric setting (devoid of free charges) it represents the physical and measurable electric potential (voltage)

$$\underline{\mathbb{E}} \coloneqq -\nabla_0\Phi \quad \text{in} \quad \mathcal{B}_0\cup\mathcal{S}_0 \quad . \tag{15}$$

The continuity condition associated with the potential is

$$[\![\Phi]\!] = 0 \quad \text{on} \quad \partial\mathcal{B}_0 \quad . \tag{16}$$

With reference to figure 1, for the electric problem the Dirichlet and Neumann boundary conditions are

$$\Phi = \overline{\Phi} \quad \text{on} \quad \partial\mathcal{B}_0^{\Phi} \quad , \quad [\![\underline{\mathbb{D}}]\!]\cdot\mathbf{N} = D_N \quad \text{on} \quad \partial\mathcal{B}_0^{\mathbb{D}} \tag{17}$$

while in contrast those of the magnetic problem are

$$\Phi = \overline{\Phi} \quad \text{on} \quad \partial\mathcal{S}_0^{\Phi} \quad , \quad \underline{\mathbb{B}}_{\infty}\cdot\mathbf{N}_{\infty} = B_{N,\infty} \quad \text{on} \quad \partial\mathcal{S}_0^{\mathbb{B}} \quad . \tag{18}$$

Given the structural similarities in equation equations (1) to (3), (9), $(11)_3$ and $(12)_3$ it is clear, that from an implementational perspective, the governing equations for the electric and magnetic problems are identical. From this point forward we consider the electric and magnetic counterparts $\{\underline{\mathbb{E}},\underline{\mathbb{H}}\}$, $\{\underline{\mathbb{D}},\underline{\mathbb{B}}\}$ and $\{\underline{\mathbb{P}},\underline{\mathbb{M}}\}$, as well as the fundamental quantities $\{\varepsilon_0,\mu_0\}$, interchangeable. However, for the purpose of post-processing for the third field the difference present in equation (4) must be taken into account. Note that in the following sections we will present the problem formulation in terms of the magnetic quantities. For detailed formulations of coupled nonlinear electro- and magneto-elasticity see, for example, [44, 57, 35, 40].

3. CONSTITUTIVE MODELLING

Since there are two distinct material domains, we consider them individually. The total energy per unit reference volume stored in electric or magnetic fields[2] [58, 42, 49] in the free space is

$$\Psi_0\left(J,\mathbf{C},\underline{\mathbb{H}}\right) \coloneqq M_0\left(J,\mathbf{C},\underline{\mathbb{H}}\right) = -\frac{\mu_0}{2}\left[J\mathbf{C}^{-1}:\underline{\mathbb{H}}\otimes\underline{\mathbb{H}}\right] \quad \text{in} \quad \mathcal{S}_0 \quad . \tag{19}$$

Following the framework described by Simo et al. [59] (also presented in, amongst many other works, [60, 55] from which the utilised notation is adopted), within the elastic body $\mathcal{B}_0$ we choose a multiplicative split of deformation gradient

$$\mathbf{F} = \left[J^{\frac{1}{3}}\mathbf{I}\right]\cdot\overline{\mathbf{F}} \tag{20}$$

where the isochoric component is $\overline{\mathbf{F}} \coloneqq J^{-\frac{1}{3}}\mathbf{F}$. We further assume a partial decoupling of the energy density function into volumetric and mixed volumetric-isochoric components such that

$$\Psi\left(J,\mathbf{C},\underline{\mathbb{H}}\right) = \Psi_0^{\text{vol}}\left(J\right) + W_0\left(J,\overline{\mathbf{C}},\underline{\mathbb{H}}\right) \quad \text{in} \quad \mathcal{B}_0 \tag{21}$$

for which Ψ_0^{vol} is a strictly convex function representing the volumetric part of the energy in the pure elastic case, W_0 is a total energy function describing the coupled material response, and $\overline{\mathbf{C}} = \overline{\mathbf{F}}^T\cdot\overline{\mathbf{F}}$ is the isochoric portion of the right Cauchy–Green tensor. Note that at this point we leave the definition of W_0 general, with its form collectively accounting for the energy stored due to elastic deformation, magnetisation and the permeating magnetic field. It is often convenient to describe the coupled effect in terms of the spatially linear response given by equation (19). For example, one may choose $W_0\left(J,\overline{\mathbf{C}},\underline{\mathbb{H}}\right) = W_0^{\text{elas}}\left(\overline{\mathbf{C}}\right) + \mu_{\text{r}}M_0\left(J,\overline{\mathbf{C}},\underline{\mathbb{H}}\right)$, with W_0^{elas} describing a purely elastic response and $\mu_{\text{r}} \geq 1$ a constant prescribing the relative permeability of the media ($\mu_{\text{r}} = 1$ represents a non-magnetisable material). Details regarding the construction of polyconvex energy functions can be found in, for example, [61, 62, 63] for elastic materials and [64, 65, 16] for coupled electro- and magneto-active polymers. The issue of material instabilities, which are of particular relevance when the electro- and magneto-strictive materials are modelled, is discussed in [66, 67, 65, 68, 64]. Furthermore, for a discussion on the validity of the assumed decomposition of the energy density function in relation to anisotropic materials, we refer the reader to the work of Sansour [69].

Using equations (19) and (21), the definition of magnetic induction and Piola–Kirchhoff stress are in general

$$\underline{\mathbb{B}} = -\frac{\partial\Psi\left(J,\mathbf{C},\underline{\mathbb{H}}\right)}{\partial\underline{\mathbb{H}}} \quad , \quad \mathbf{S} = 2\frac{\partial\Psi\left(J,\mathbf{C},\underline{\mathbb{H}}\right)}{\partial\mathbf{C}} \quad , \tag{22}$$

and we implicitly define the polarisation/magnetisation vector through equation (4).

[2]For the magnetic problem in particular, the natural description of the free field energy is given in terms of the magnetic induction. A Legendre transformation, which is necessary to change the independent variable, results in the form given in equation (19). Further details on this point are given in [56] and references therein.

4. VARIATIONAL FORMULATION

Due to the need to simulate near incompressible media, it is generally not feasible to utilise a standard approach with a low-order displacement ansatz to discretise the elastic part of the problem. This is due to the tendency of these low-order finite elements to exhibit volumetric locking in quasi-incompressible solids (as well as shear locking in bending dominated problems). However, the use of higher-order elements is often not preferred in practical applications due to their added computational expense.

Application of the Veubeke-Hu-Washizu principle [70] regularly forms the cornerstone in the development of mixed methods applied to the finite element approach to prevent the occurrence of locking in elastic problems. Based on the seminal work by Nagtegaal et al. [71], Simo et al. [59] (and also [72, 60]) presented a formulation for non-linear quasi-incompressible elasticity that utilises two additional scalar fields. Although it has some drawbacks, it offers a balance between computational expense and implementational simplicity [73] versus other mixed methods [74, 75, 64] and alternatives approaches. Hu-Washizu mixed formulations for the coupled problem have been successfully adopted by Ask et al. [76, 22, 77], Jabareen [78], and Ortigosa and Gil [28], albeit for conditions that exclude the free space.

In this work we use a mixed variational approach to derive the weak form of the governing equations. Inspired by the work of Simo et al. [59] and Ask et al. [77], we define the total potential energy functional

$$\begin{aligned}\Pi = \Pi^{\text{int}} - \Pi^{\text{ext}} = &\int_{\mathcal{B}_0} \left[\Psi_0^{\text{vol}}\left(\widetilde{J}\right) + W_0\left(\widetilde{J}, \overline{\mathbf{C}}, \underline{\mathbb{H}}\right) + \widetilde{p}\left[J - \widetilde{J}\right]\right] dV + \int_{\mathcal{S}_0} M_0\left(J, \mathbf{C}, \underline{\mathbb{H}}\right) dV \\ &- \int_{\mathcal{B}_0} \boldsymbol{\varphi} \cdot \mathbf{b}_0 \, dV - \int_{\partial\mathcal{B}_0^{\mathbf{t}}} \boldsymbol{\varphi} \cdot \mathbf{t}_0 \, dA - \int_{\partial\mathcal{S}_0^{\mathbb{B}}} \Phi\left[\underline{\mathbb{B}}_\infty \cdot \mathbf{N}_\infty\right] dA \quad ,\end{aligned} \tag{23}$$

wherein the third term in the integral over the solid body in equation (23) penalises the difference between the point-wise volumetric Jacobian $J = J(\boldsymbol{\varphi}) = \det(\mathbf{F})$ and the dilatation $\widetilde{J}$. We recognise the Lagrange multiplier $\widetilde{p}$ as the pressure response, related to the hydrostatic pressure by $\widetilde{p} = -p^{\text{hyd}}$. From equation (23) we discern that there are three unknown elastic field variables and one related to the electric or magnetic problem. Note that, unlike Simo and Taylor [72], we do not directly impose incompressibility conditions via a penalty or Lagrange multiplier method, but will rather prescribe a bulk modulus that is representative of a near-incompressible material.

The stationary (saddle-)point [79] $\min\limits_{\boldsymbol{\varphi},\widetilde{J}} \max\limits_{\widetilde{p},\Phi} \Pi \;\Rightarrow\; \delta\Pi = 0$ defines the equilibrium solution for the boundary value problem. Using the Gâteaux derivative

$$\delta\Pi = \left[\mathrm{D}_{\delta\boldsymbol{\varphi}}\Pi^{\text{int}} + \mathrm{D}_{\delta\widetilde{p}}\Pi^{\text{int}} + \mathrm{D}_{\delta\widetilde{J}}\Pi^{\text{int}} + \mathrm{D}_{\delta\Phi}\Pi^{\text{int}}\right] - \left[\mathrm{D}_{\delta\boldsymbol{\varphi}}\Pi^{\text{ext}} + \mathrm{D}_{\delta\Phi}\Pi^{\text{ext}}\right] \quad , \tag{24}$$

the components of the first variation are

$$\mathrm{D}_{\delta\boldsymbol{\varphi}}\Pi^{\text{int}} = \int_{\mathcal{B}_0} \delta\mathbf{E} : \left[\overline{\mathbf{S}}^{\text{tot}} + \widetilde{p}J\mathbf{C}^{-1}\right]\, dV + \int_{\mathcal{S}_0} \delta\mathbf{E} : \mathbf{S}^{\text{max}}\, dV \quad , \tag{25a}$$

$$\mathrm{D}_{\delta\widetilde{p}}\Pi^{\text{int}} = \int_{\mathcal{B}_0} \delta\widetilde{p}\left[J - \widetilde{J}\right]\, dV \quad , \quad \mathrm{D}_{\delta\widetilde{J}}\Pi^{\text{int}} = \int_{\mathcal{B}_0} \delta\widetilde{J}\left[\frac{\partial\Psi_0^{\text{vol}}}{\partial\widetilde{J}} + \frac{\partial W_0}{\partial\widetilde{J}} - \widetilde{p}\right]\, dV \quad , \tag{25b}$$

$$\mathrm{D}_{\delta\Phi}\Pi^{\text{int}} = -\int_{\mathcal{B}_0} \delta\underline{\mathbb{H}} \cdot \underline{\mathbb{B}}^{\text{tot}}\, dV - \int_{\mathcal{S}_0} \delta\underline{\mathbb{H}} \cdot \underline{\mathbb{B}}^{\text{max}}\, dV \quad , \tag{25c}$$

$$\mathrm{D}_{\delta\boldsymbol{\varphi}}\Pi^{\text{ext}} = -\int_{\mathcal{B}_0} \delta\boldsymbol{\varphi}\cdot\mathbf{b}_0\, dV - \int_{\partial\mathcal{B}_0^{\mathbf{t}}} \delta\boldsymbol{\varphi}\cdot\mathbf{t}_0\, dA \quad , \quad \mathrm{D}_{\delta\Phi}\Pi^{\text{ext}} = -\int_{\partial\mathcal{S}_0^{\mathbb{B}}} \delta\Phi\left[\underline{\mathbb{B}}_\infty \cdot \mathbf{N}_\infty\right]\, dA \quad , \tag{25d}$$

with

$$\delta\mathbf{E} = \text{sym}\left[\mathbf{F}^T\cdot\delta\mathbf{F}\right] \quad , \quad \delta\mathbf{F} = \nabla_0\delta\boldsymbol{\varphi} \quad , \quad \delta\underline{\mathbb{H}} = -\nabla_0\delta\Phi \quad . \tag{26}$$

From equation (22), the total stress and induction within the elastic body are expressed as

$$\mathbf{S}^{\text{tot}} = \overline{\mathbf{S}}^{\text{tot}} + \widetilde{p}J\mathbf{C}^{-1} \quad , \quad \overline{\mathbf{S}}^{\text{tot}} = 2\frac{\partial W_0}{\partial\mathbf{C}} = \overline{\boldsymbol{\mathcal{P}}} : \left[2\frac{\partial W_0}{\partial\overline{\mathbf{C}}}\right] \quad , \quad \underline{\mathbb{B}}^{\text{tot}} = -\frac{\partial W_0}{\partial\underline{\mathbb{H}}} \tag{27}$$

with the referential projection tensor defined as [54]

$$\overline{\boldsymbol{\mathcal{P}}} \coloneqq \frac{\partial\overline{\mathbf{C}}}{\partial\mathbf{C}} = J^{-\frac{2}{3}}\left[\boldsymbol{\mathcal{I}} - \frac{1}{3}\mathbf{C}\otimes\mathbf{C}^{-1}\right] \quad . \tag{28}$$

The symmetric fourth-order identity tensor is $\boldsymbol{\mathcal{I}} = \frac{1}{2}\left[\mathbf{I}\overline{\otimes}\mathbf{I} + \mathbf{I}\overline{\overline{\otimes}}\mathbf{I}\right]$, where $\mathbf{I}$ is the referential identity tensor and for which we define the non-standard tensor outer products $\boldsymbol{\mathcal{C}} = \mathbf{A}\overline{\otimes}\mathbf{B} \rightarrow \mathcal{C}_{ijkl} = A_{ik}B_{jl}$ and $\boldsymbol{\mathcal{C}} = \mathbf{A}\overline{\overline{\otimes}}\mathbf{B} \rightarrow \mathcal{C}_{ijkl} = A_{il}B_{jk}$. As it is a non-magnetisable medium, the counterpart stress and induction in the free space reduce to the Maxwell contributions

$$\mathbf{S}^{\text{max}} = 2\frac{\partial M_0}{\partial\mathbf{C}} \quad , \quad \underline{\mathbb{B}}^{\text{max}} = -\frac{\partial M_0}{\partial\underline{\mathbb{H}}} \quad . \tag{29}$$

The relationship between the developed weak form and the strong form is collectively detailed in [45, 80] (for a more simplified form of the electro- and magneto-static problems) and [55] (for the three-field elastostatic problem).

From equations (25) it is noted that the space in which the variations must lie are

$$\delta\Phi \in \mathcal{H}^1\left(\overline{\mathcal{B}_0 \cup \mathcal{S}_0}\right) \quad , \quad \delta\boldsymbol{\varphi} \in \mathcal{H}^1\left(\overline{\mathcal{B}_0}\right) \quad , \quad \delta\widetilde{p}, \delta\widetilde{J} \in \mathcal{L}^2\left(\overline{\mathcal{B}_0}\right) \tag{30}$$

with constraints

$$\delta\Phi = 0 \quad \text{on} \quad \partial\mathcal{B}_0^\Phi \quad \text{and} \quad \partial\mathcal{S}_0^\Phi \quad , \quad \delta\boldsymbol{\varphi} = \mathbf{0} \quad \text{on} \quad \partial\mathcal{B}_0^{\boldsymbol{\varphi}} \cup \left[\overline{\mathcal{S}_0}\backslash\Gamma_0^{\mathcal{BS}}\right] \quad , \tag{31}$$

where $\Gamma_0^{\mathcal{BS}} = \overline{\mathcal{S}_0} \cap \overline{\mathcal{B}_0}$ indicates the boundary of the solid exposed to the free space. We note that the variation of the displacement degrees-of-freedom is set to vanish not only on the Dirichlet boundaries of the solid body, but also in the region of the free space not overlapping with the body. This is sensible as the free space naturally offers no (elastic) resistance to the movement of the solid body at low deformation rates (when viscous forces are negligible).

As the coupled problem is nonlinear, the linearisation of equations (25) will be required as part of an iterative numerical solution scheme. This is provided in appendix A.

5. FINITE ELEMENT DISCRETISATION

In order to solve the boundary value problem, we employ the Galerkin finite-element method that, for this problem, ultimately leads to a symmetric and square linear system. As to best replicate its implementation, we define vector- $(\mathbf{N})$ and scalar- (N, M, Q) valued shape functions for each global degree-of-freedom. Using these, the discretisation of the unknown fields and their variations is expressed as

$$\begin{aligned} \boldsymbol{\varphi}(\mathbf{X}) &\approx \sum_I \varphi^I \mathbf{N}^I(\mathbf{X}) \quad , \quad \Phi(\mathbf{X}) \approx \sum_I \Phi^I N^I(\mathbf{X}) \quad , \\ \widetilde{p}(\mathbf{X}) &\approx \sum_I \widetilde{p}^I M^I(\mathbf{X}) \quad , \quad \widetilde{J}(\mathbf{X}) \approx \sum_I \widetilde{J}^I Q^I(\mathbf{X}) \quad , \end{aligned} \tag{32}$$

with corresponding gradients

$$\nabla_0 \boldsymbol{\varphi}(\mathbf{X}) \approx \sum_I \varphi^I \nabla_0 \mathbf{N}^I(\mathbf{X}) \quad , \quad \nabla_0 \Phi(\mathbf{X}) \approx \sum_I \Phi^I \nabla_0 N^I(\mathbf{X}) \quad . \tag{33}$$

From equation (24), the discretised form of the first variation is therefore

$$\begin{aligned} \delta\Pi = \delta\varphi^I \underbrace{\left[\int_{\mathcal{B}_0} \operatorname{sym}\left[\mathbf{F}^T \cdot \nabla_0 \mathbf{N}^I\right] : \left[\overline{\mathbf{S}}^{\text{tot}} + \widetilde{p} J \mathbf{C}^{-1}\right] dV + \int_{\mathcal{S}_0} \operatorname{sym}\left[\mathbf{F}^T \cdot \nabla_0 \mathbf{N}^I\right] : \mathbf{S}^{\max} dV \right]}_{\left[\delta\Pi_{\boldsymbol{\varphi}}^{\text{int}}\right]^I} \\ + \delta\varphi^I \underbrace{\left[- \int_{\mathcal{B}_0} \mathbf{N}^I \cdot \mathbf{b}_0 \, dV - \int_{\partial\mathcal{B}_0^{\mathbf{t}}} \mathbf{N}^I \cdot \mathbf{t}_0 \, dA \right]}_{\left[\delta\Pi_{\boldsymbol{\varphi}}^{\text{ext}}\right]^I} + \delta\widetilde{p}^I \underbrace{\int_{\mathcal{B}_0} M^I \left[J - \widetilde{J}\right] dV}_{\left[\delta\Pi_{\widetilde{p}}\right]^I} \\ + \delta\widetilde{J}^I \underbrace{\int_{\mathcal{B}_0} Q^I \left[\frac{\partial \Psi_0^{vol}}{\partial \widetilde{J}} + \frac{\partial W_0}{\partial \widetilde{J}} - \widetilde{p}\right] dV}_{\left[\delta\Pi_{\widetilde{J}}\right]^I} + \delta\Phi^I \underbrace{\left[\int_{\mathcal{B}_0 \cup \mathcal{S}_0} \nabla_0 N^I \cdot \underline{\mathbb{B}} \, dV - \int_{\partial\mathcal{S}_0^{\mathbb{B}}} N^I \left[\underline{\mathbb{B}}_\infty \cdot \mathbf{N}_\infty\right] dA \right]}_{\left[\delta\Pi_{\Phi}\right]^I} \end{aligned} \tag{34}$$

from which the residual for each degree-of-freedom is expressed as

$$r^I = \delta\Pi^I_{\boldsymbol{\varphi}} + \delta\Pi^I_{\widetilde{p}} + \delta\Pi^I_{\widetilde{J}} + \delta\Pi^I_{\Phi} \tag{35}$$

The discretised expression for the linearisation follows similarly.

For the purpose of computational convenience, we introduce the numerical subdomain $\overline{\mathcal{S}_0^{\mathcal{B},h}} \subset \overline{\mathcal{S}_0^h}$ such that $\overline{\Gamma_0^{\mathcal{BS},h}} = \overline{\mathcal{B}_0^h} \cap \overline{\mathcal{S}_0^{\mathcal{B},h}}$. As is shown in figure 2, for the discrete problem this is a single layer of cells extending outwards from the elastic body $\mathcal{B}_0^h$ into the free space $\mathcal{S}_0^h$, such that all cells in $\mathcal{S}_0^{\mathcal{B},h}$ share at least one vertex with the cells in $\mathcal{B}_0^h$. Using this approach we may reduce the integration domain for the Maxwell stress contributions in equation (34) from $\mathcal{S}_0^h$ to $\mathcal{S}_0^{\mathcal{B},h}$. This is motivated by the observation that this stress has a detectable influence only on $\mathcal{B}_0$ and by the constraint requirements for $\delta\boldsymbol{\varphi}$ listed in equation (31).

We subsequently employ a reduced discretisation for each unknown field of the presented problem. In table I we outline the finite element spaces for each field applied to each subdomain. Given the domain of integration for the solid, the basis functions M, Q need only have support on $\overline{\mathcal{B}_0^h}$ while N require support on $\overline{\mathcal{B}_0^h \cup \mathcal{S}_0^h}$. As motivated above we can *a priori* remove any displacement degrees-of-freedom[3] from $\overline{\mathcal{S}_0^h} \backslash \overline{\mathcal{S}_0^{\mathcal{B},h}}$. This compact discretisation leads to the smallest linear problem that approximates the fundamental governing equations. The benefit of such an approach would be most visible on problems with large domains and a large number of degrees-of-freedom in the free space.

In the example problems for the coupled problem we employ continuous trilinear (order 1) Lagrange finite elements to approximate each component of the displacement field as well as for the potential field. The use of continuous elements ensures that the tangential continuity, compatibility and potential continuity conditions, respectively listed in $(3)_{1,3}$, (5) and (16), are fulfilled as the gradients of the fields are curl-free. Motivated by the necessity to satisfy the Ladyzenskaja-Babuška-Brezzi (LBB) conditions[4], identical discontinuous constant elements are used for the pressure response and dilatation fields.

6. SOLUTION OF LINEAR ITERATION STEP

As the variations $\delta\boldsymbol{\varphi}, \delta\widetilde{p}, \delta\widetilde{J}, \delta\Phi$ are arbitrary, a discretised system of linear equations which is valid for all variations can be formed from the linearisation of equation (34). At any given time t and

[3]Within $\mathcal{B}_0$, the deformation gradient results from displacement of the elastic body. However, in the free space the description of the Lagrangian movement of mesh is arbitrary (although $\det \mathbf{F} > 0$ to ensure an invertible mapping between the referential and spatial configurations). In $\mathcal{S}_0$, $\mathbf{F}$ is therefore provided by the solution of the auxiliary problem presented in section 7 so that the mesh quality in the current configuration $\mathcal{S}_t$ is preserved.

[4]The chosen discretisation is based on the well known $Q1 - P0 - P0$ solid element which is known, for the lowest possible order $n = 1$, not to strictly satisfy the LBB conditions [81]. In practice, however, this choice has been shown to be robust [59, 82, 72, 60].

Newton iterate n the discrete form of algebraic equations are

$$\begin{bmatrix} \mathbf{K}_{\boldsymbol{\varphi}\boldsymbol{\varphi}} & \mathbf{K}_{\boldsymbol{\varphi}\widetilde{p}} & \mathbf{K}_{\boldsymbol{\varphi}\widetilde{J}} & \mathbf{K}_{\boldsymbol{\varphi}\Phi} \\ \mathbf{K}_{\widetilde{p}\boldsymbol{\varphi}} & \mathbf{0} & \mathbf{K}_{\widetilde{p}\widetilde{J}} & \mathbf{0} \\ \mathbf{K}_{\widetilde{J}\boldsymbol{\varphi}} & \mathbf{K}_{\widetilde{J}\widetilde{p}} & \mathbf{K}_{\widetilde{J}\widetilde{J}} & \mathbf{K}_{\widetilde{J}\Phi} \\ \mathbf{K}_{\Phi\boldsymbol{\varphi}} & \mathbf{0} & \mathbf{K}_{\Phi\widetilde{J}} & \mathbf{K}_{\Phi\Phi} \end{bmatrix} \begin{bmatrix} \Delta\mathbf{d}_{\boldsymbol{\varphi}} \\ \Delta\mathbf{d}_{\widetilde{p}} \\ \Delta\mathbf{d}_{\widetilde{J}} \\ \Delta\mathbf{d}_{\Phi} \end{bmatrix} = \begin{bmatrix} \mathbf{f}_{\boldsymbol{\varphi}} \\ \mathbf{f}_{\widetilde{p}} \\ \mathbf{f}_{\widetilde{J}} \\ \mathbf{f}_{\Phi} \end{bmatrix} \quad \Rightarrow \quad \mathbf{K}\cdot\Delta\mathbf{d} = \mathbf{f} = -\mathbf{r} \tag{36}$$

where $\mathbf{r} \to \mathbf{0}$ is the residual vector given in equation (35) and $\Delta\mathbf{d}$ is the iterative increment with which we compute the solution update for each iteration n by

$$\mathbf{d}_{n+1} = \mathbf{d}_n + \Delta\mathbf{d} \quad . \tag{37}$$

In general, possible approaches to solving such a system of equations include (i) the use of a direct solver, (ii) construction of a global preconditioner for use with a global iterative solver, and (iii) exploitation of the tangent matrix's block-structure to sequentially solve for each variable.

Solving the saddle-point problem arising from the discretisation and linearisation of the boundary scheme poses several challenges [79]. Most apparent is that, since $\widetilde{p}$ is a Lagrange multiplier, there is no pressure-pressure coupling ($\mathbf{K}_{\widetilde{p}\widetilde{p}} = \mathbf{0}$) which renders the global system singular [83]. The properties of the symmetric blocks $\mathbf{K}_{\boldsymbol{\varphi}\boldsymbol{\varphi}}$ and $\mathbf{K}_{\Phi\Phi}$ are less certain as they depend on the chosen constitutive models and their parameters, as well as the electric/magnetic field in the free space. Consider the decomposition

$$\mathbf{K}_{\boldsymbol{\varphi}\boldsymbol{\varphi}} = \begin{bmatrix} \mathbf{K}^{B,B}_{\boldsymbol{\varphi}\boldsymbol{\varphi}} & \mathbf{K}^{B,T}_{\boldsymbol{\varphi}\boldsymbol{\varphi}} & 0 \\ \mathbf{K}^{T,B}_{\boldsymbol{\varphi}\boldsymbol{\varphi}} & \mathbf{K}^{T,T}_{\boldsymbol{\varphi}\boldsymbol{\varphi}} & \mathbf{K}^{T,S}_{\boldsymbol{\varphi}\boldsymbol{\varphi}} \\ 0 & \mathbf{K}^{S,T}_{\boldsymbol{\varphi}\boldsymbol{\varphi}} & \mathbf{K}^{S,S}_{\boldsymbol{\varphi}\boldsymbol{\varphi}} \end{bmatrix} \quad , \quad \mathbf{K}_{\Phi\Phi} = \begin{bmatrix} \mathbf{K}^{B,B}_{\Phi\Phi} & \mathbf{K}^{B,T}_{\Phi\Phi} & 0 \\ \mathbf{K}^{T,B}_{\Phi\Phi} & \mathbf{K}^{T,T}_{\Phi\Phi} & \mathbf{K}^{T,S}_{\Phi\Phi} \\ 0 & \mathbf{K}^{S,T}_{\Phi\Phi} & \mathbf{K}^{S,S}_{\Phi\Phi} \end{bmatrix} \tag{38}$$

with $B = \mathcal{B}_0^h \backslash \Gamma_0^{\mathcal{BS},h}$, $T = \Gamma_0^{\mathcal{BS},h}$ and $S = \mathcal{S}_0^h \backslash \Gamma_0^{\mathcal{BS},h}$. Derived from the concave transformed energy function given by equation (19), both of the free space tangent contributions $\mathbf{K}^{S,S}_{\boldsymbol{\varphi}\boldsymbol{\varphi}}$ and $\mathbf{K}^{S,S}_{\Phi\Phi}$ are negative-definite. The electric/magnetic tangent within the body $\mathbf{K}^{B,B}_{\Phi\Phi}$ may either be positive or negative-definite depending on the constitutive law and parameters (for example, paramagnetic versus diamagnetic materials). Ideally $\mathbf{K}^{B,B}_{\boldsymbol{\varphi}\boldsymbol{\varphi}}$ is always positive-definite, which would be the case if Ψ_0 is polyconvex. However, due to the electric/magnetic contributions (for example, simply that given in equation (19)) this no longer necessarily holds and is the source of the material instabilities referred to in section 3. They correspond to observable physical phenomena in electro-/magneto-strictive materials; for example, electric breakdown in capacitors. At low magnetic fields and high deformation the elastic stiffness dominates, while at high magnetic fields and low deformation the contributions from the electric/magnetic terms dominate, indicating that the material can no longer resist the induced ponderomotive forces. This effect is exacerbated by the presence of the surrounding free space. Although the tangent stiffness matrix $\mathbf{K}^{S,S}_{\boldsymbol{\varphi}\boldsymbol{\varphi}}$ can be ignored (because $\delta\boldsymbol{\varphi} = 0$ on $\mathcal{S}_0^h$), that of $\mathbf{K}^{T,T}_{\boldsymbol{\varphi}\boldsymbol{\varphi}}$ must remain. For the degrees-of-freedom on the body's boundary, $\mathbf{K}^{T,T}_{\boldsymbol{\varphi}\boldsymbol{\varphi}}$ includes contributions from the body (positive-definite) and free space (negative-definite). It is expected that at low electric/magnetic fields the former dominates but at high electric/magnetic fields the latter contribution is expected to dominate, potentially leading to numerical instabilities.

Wishing to investigate the third solution strategy, we first restrict ourselves to energy functions of the form $W_0 = W_0\left(\overline{\mathbf{C}}, \underline{\mathbb{H}}\right)$ to describe the coupled response of quasi-incompressible media. This implies that the stored energy due to material dilation as a response to the applied electric/magnetic field is negligible and contributions of the form given by equation (19) can be transformed to

$$\overline{M}_0\left(\overline{\mathbf{C}}, \underline{\mathbb{H}}\right) = -\frac{\mu_0}{2}\left[\overline{\mathbf{C}}^{-1} : \underline{\mathbb{H}} \otimes \underline{\mathbb{H}}\right] \quad \text{in} \quad \mathcal{B}_0 \tag{39}$$

within the near incompressible body. This simplifies the structure of equation (36) slightly as there is no resulting coupling of the form $\mathbf{K}_{\boldsymbol{\varphi}\widetilde{J}}, \mathbf{K}_{\widetilde{J}\boldsymbol{\varphi}}$ nor $\mathbf{K}_{\widetilde{J}\Phi}, \mathbf{K}_{\Phi\widetilde{J}}$. To increase the stability of the problem we neglect the material tangent of the Maxwell contribution to $\mathbf{K}^{T,T}_{\boldsymbol{\varphi}\boldsymbol{\varphi}}$. It will be later demonstrated that this does not necessarily lead to inferior convergence rates in the nonlinear solver for the range of stable electric/magnetic fields.

Using Gaussian elimination of the full block system, the linear problem for the displacement update is expressed as

$$\begin{aligned}\underbrace{\left[\mathbf{K}_{\boldsymbol{\varphi}\boldsymbol{\varphi}} + \mathbf{K}_{\boldsymbol{\varphi}\widetilde{p}}\mathbf{K}^{-1}_{\widetilde{J}\widetilde{p}}\mathbf{K}_{\widetilde{J}\widetilde{J}}\mathbf{K}^{-1}_{\widetilde{p}\widetilde{J}}\mathbf{K}_{\widetilde{p}\boldsymbol{\varphi}} - \mathbf{K}_{\boldsymbol{\varphi}\Phi}\,\mathbf{K}^{-1}_{\Phi\Phi}\,\mathbf{K}_{\Phi\boldsymbol{\varphi}}\right]}_{\mathbf{S}}\Delta\mathbf{d}_{\boldsymbol{\varphi}} \\ = \underbrace{\mathbf{f}_{\boldsymbol{\varphi}} - \mathbf{K}_{\boldsymbol{\varphi}\widetilde{p}}\mathbf{K}^{-1}_{\widetilde{J}\widetilde{p}}\left[\mathbf{f}_{\widetilde{J}} - \mathbf{K}_{\widetilde{J}\widetilde{J}}\mathbf{K}^{-1}_{\widetilde{p}\widetilde{J}}\mathbf{f}_{\widetilde{p}}\right] - \mathbf{K}_{\boldsymbol{\varphi}\Phi}\mathbf{K}^{-1}_{\Phi\Phi}\mathbf{f}_{\Phi}}_{\mathbf{f}} \quad .\end{aligned} \tag{40}$$

where the incremental updates for the scalar potential, dilatation and pressure response fields are respectively given by

$$\Delta\mathbf{d}_{\Phi} = \mathbf{K}^{-1}_{\Phi\Phi}\left[\mathbf{f}_{\Phi} - \mathbf{K}_{\Phi\boldsymbol{\varphi}}\,\Delta\mathbf{d}_{\boldsymbol{\varphi}}\right] \quad , \tag{41}$$

$$\Delta\mathbf{d}_{\widetilde{J}} = \mathbf{K}^{-1}_{\widetilde{p}\widetilde{J}}\left[\mathbf{f}_{\widetilde{p}} - \mathbf{K}_{\widetilde{p}\boldsymbol{\varphi}}\Delta\mathbf{d}_{\boldsymbol{\varphi}}\right] \quad , \tag{42}$$

$$\Delta\mathbf{d}_{\widetilde{p}} = \mathbf{K}^{-1}_{\widetilde{J}\widetilde{p}}\left[\mathbf{f}_{\widetilde{J}} - \mathbf{K}_{\widetilde{J}\widetilde{J}}\Delta\mathbf{d}_{\widetilde{J}}\right] \quad . \tag{43}$$

Alternatively, one may also exploit the discontinuous fields $\widetilde{p}$, $\widetilde{J}$ and perform static condensation to remove these degrees-of-freedom from the global system. From this, a condensed form of the linear problem is

$$\underbrace{\left[\widetilde{\mathbf{K}}_{\boldsymbol{\varphi}\boldsymbol{\varphi}} - \mathbf{K}_{\boldsymbol{\varphi}\Phi}\,\mathbf{K}^{-1}_{\Phi\Phi}\,\mathbf{K}_{\Phi\boldsymbol{\varphi}}\right]}_{\widetilde{\mathbf{S}}}\Delta\mathbf{d}_{\boldsymbol{\varphi}} = \underbrace{\widetilde{\mathbf{f}}_{\boldsymbol{\varphi}} - \mathbf{K}_{\boldsymbol{\varphi}\Phi}\mathbf{K}^{-1}_{\Phi\Phi}\mathbf{f}_{\Phi}}_{\widetilde{\mathbf{f}}} \quad , \tag{44}$$

where the augmented stiffness matrix and right-hand side vector contributions are

$$\widetilde{\mathbf{K}}_{\boldsymbol{\varphi}\boldsymbol{\varphi}} = \mathbf{K}_{\boldsymbol{\varphi}\boldsymbol{\varphi}} + \mathbf{K}_{\boldsymbol{\varphi}\widetilde{p}}\overline{\mathbf{K}}_{\widetilde{p}\widetilde{p}}\mathbf{K}_{\widetilde{p}\boldsymbol{\varphi}} \quad , \quad \widetilde{\mathbf{f}}_{\boldsymbol{\varphi}} = \mathbf{f}_{\boldsymbol{\varphi}} - \mathbf{K}_{\boldsymbol{\varphi}\widetilde{p}}\left[\mathbf{K}^{-1}_{\widetilde{J}\widetilde{p}}\mathbf{f}_{\widetilde{J}} - \overline{\mathbf{K}}_{\widetilde{p}\widetilde{p}}\mathbf{f}_{\widetilde{p}}\right] \quad , \tag{45a}$$

for which the auxiliary matrix, which retains a block-sparse structure, is given by

$$\overline{\mathbf{K}}_{\widetilde{p}\widetilde{p}} \coloneqq \mathbf{K}^{-1}_{\widetilde{J}\widetilde{p}}\mathbf{K}_{\widetilde{J}\widetilde{J}}\mathbf{K}^{-1}_{\widetilde{p}\widetilde{J}} \quad . \tag{45b}$$

Note that the solutions to the two strategies

$$\Delta \mathbf{d}_{\boldsymbol{\varphi}} = \widetilde{\mathbf{S}}^{-1}\widetilde{\mathbf{f}} \equiv \mathbf{S}^{-1}\mathbf{f} \tag{46}$$

are equivalent but their implementation differs.

The discrete problem is implemented and solved using the open-source finite element library `deal.II` [84, 85] in conjunction with the Trilinos [86, 87] linear algebra suite. The framework used to implement the discretisation strategy described in section 5 is detailed in [88]. Further details related to the formulation of the linear solution procedure and the choice of linear solvers are given in appendix B.

7. LARGE DEFORMATIONS AND THE SURROUNDING FREE SPACE

In problems involving both magneto-elastic bodies and the simulation of the free space, typically a fine mesh is used at the solid-free space interface to accurately capture the locally steep electromagnetic field gradients. Without some imposition of a fictitious motion to the free space mesh, impingement by the body on the fine adjacent cells would occur at finite deformations likely rendering the displacement map in $\mathcal{S}_0^{\mathcal{B},h}$, at the very least, non-invertible. In large deformation problems it is therefore typical that a mesh-update algorithm be employed to prevent this. The Laplace update method has found use in general fluid mechanics problems [89, 90], as well as those related to magneto-active polymers [26]. An elasticity-based approach to the mesh-motion problem has also been explored in fluid simulation [91, 92] and magneto-elasticity [18] problems. An alternative method, as described by Knupp et al. [93], involves the movement of mesh points as to retain or improve the computational properties of the discretisation.

As described in section 5, the elastic degrees-of-freedom in the free space had been removed from the primary coupled problem. We therefore compose a secondary problem to compute a suitable deformation map $\boldsymbol{\varphi}$ in $\mathcal{S}_0$. These two problems are solved in a staggered manner, with the auxiliary problem only being evaluated if some measure of the displacement update of the primary problem is larger than a prescribed threshold. In the current implementation we adopt a conservative approach and perform the update if $|\Delta \mathbf{d}_{\boldsymbol{\varphi}}|_\infty \in \mathcal{B}_0$ is greater than $1\,\%$ of the smallest mesh element diameter. If the secondary problem is not evaluated, then only the displacement degrees-of-freedom on $\Gamma_0^{\mathcal{BS}}$ are incrementally updated thereby ensuring that $\boldsymbol{\varphi}$ in $\mathcal{S}_0^{\mathcal{B},h}$ is synchronised for both the primary and auxiliary problems. The resulting map is then used in the computation of equation (34), its linearisation and spatial quantities defined in $\mathcal{S}_t$.

Given that a (reusable) finite-deformation elastic framework has been developed for the primary coupled problem, there are two relevant update methodologies that are physically-based, simple to implement and compatible with this framework. Presented in strong form, the vector-valued Laplace and static linear elasticity equation, along with their constitutive laws, are respectively

$$\nabla_0 \cdot [\boldsymbol{\mathcal{K}} \nabla_0 \boldsymbol{\varphi}] = \mathbf{0} \quad \text{on} \quad \mathcal{S}_0 \quad , \quad \boldsymbol{\mathcal{K}}(\mathbf{X}) = c(\mathbf{X})\boldsymbol{\mathcal{I}} \quad , \tag{47}$$

$$\nabla_0 \cdot [\boldsymbol{\mathcal{K}} [\nabla_0 \boldsymbol{\varphi}]^s] = \mathbf{0} \quad \text{on} \quad \mathcal{S}_0 \quad , \quad \boldsymbol{\mathcal{K}}(\mathbf{X}) = \mu(\mathbf{X})\boldsymbol{\mathcal{I}} + \lambda(\mathbf{X})\,\mathbf{I}\otimes\mathbf{I} \quad . \tag{48}$$

Spatially dependent material constants are denoted by c, μ, and λ. The discretisation of $\mathcal{S}_0$ by finite elements is detailed in table I. The boundary conditions associated with the auxiliary problem are

$$\boldsymbol{\varphi} = \overline{\boldsymbol{\varphi}} \quad \text{on} \quad \Gamma_0^{\mathcal{BS}} \quad \text{and} \quad \boldsymbol{\varphi} = \overline{\overline{\boldsymbol{\varphi}}} \quad \text{on} \quad \partial\mathcal{S}_0 \quad , \tag{49}$$

for which the displacement on the solid-free space interface is prescribed by the solution of the primary coupled problem, denoted as $\overline{\boldsymbol{\varphi}}$. There exists no limitation on the movement of degrees-of-freedom within the free space domain, except that material domains with different magnetic permeabilities should retain their original topology. Mesh sliding is allowed on the far-field boundary, but the shape of the geometry must remain the same while a electric or magnetic load is applied.

We propose that, as a more general expression of the above, equation $(48)_1$ be used in conjunction with a local isotropic stiffness tensor of the form

$$\boldsymbol{\mathcal{K}}(\mathbf{X}) = k(\mathbf{X})\left[[1-\alpha]\,\boldsymbol{\mathcal{I}} + \alpha \mathbf{I}\otimes\mathbf{I}\right] \tag{50}$$

where $k(\mathbf{X}) > 0$ is a function governing the effective stiffness magnitude at the given coordinate position.

The value $-1 \leq \alpha \leq 1$ is a blending parameter that effectively prescribes the Poisson ratio $\nu^* = \dfrac{\alpha}{2}$ for the fictitious elastic media[5]. Some noteworthy choices of the blending parameter are: $\alpha = 0$ describes a highly compressible material ($\nu^* = 0$), $\alpha \to 1$ describes a material with increasing incompressibility ($\nu^* \to 0.5$) and $\alpha = 1$ behaves like an "incompressible" media, with zero shear modulus but a finitely bounded Lamé parameter. When comparing these governing equations along with their associated constitutive laws, it is observed that setting $\alpha = -1$ reduces the elasticity equations to the Laplace equations[6] given in equation (47).

For the stiffness function $k(\mathbf{X})$, we evaluate the options listed by Jasak and Tukovićć [89] as being effective candidates in the update of meshes in airfoil simulations. Given a certain metric $d(\mathbf{X})$ and a exponent p, we may choose either a homogeneous, power law or exponential law for the stiffness

$$k = \overline{k} = 1 \quad \text{or} \quad k(d) = d^{-p} \quad \text{or} \quad k(d) = \exp(-d\,p) \quad . \tag{51}$$

Here we note that, for the last two choices of k, there is an inverse relationship between the stiffness and the given metric d. In this work, we investigate two metrics. The first is the cell diameter, which is defined as the value of the largest diagonal of the undeformed cell containing $\mathbf{X}$. The principle behind this choice of metric is that the smaller the cell, naturally the less relative motion between its vertices can be accommodated before it becomes significantly deformed. The second metric is the distance from $\mathbf{X}$ to the nearest solid-body vertex, again measured in the reference configuration. Thus the movement of the cells adjacent to the solid should in concept be translation dominated,

[5]This can be directly shown through the identity $\nu = \dfrac{\lambda}{2(\lambda+\mu)}$ by noting the similarities between equation (50) and the classical description of the isotropic linear elastic stiffness modulus given in equation $(48)_2$.

[6]Shown in appendix C, this may be deduced by substituting equation (50) into equation $(48)_1$ and comparing the result to the static Navier–Cauchy displacement equations, $[\lambda+\mu]\,\nabla[\nabla\cdot\boldsymbol{\varphi}] + \mu\nabla\cdot[\nabla\boldsymbol{\varphi}] = \mathbf{0}$, which demonstrates that the linear elastic problem can be written as a superposition of a "convective" (vector Laplacian) and a "diffusive" quantity.

while those in the far-field deform freely. However, it should be noted that for this choice there is an underlying assumption that all of the smallest cells are located in the near vicinity of the solid body, as would be found in a boundary-layer mesh for fluid simulations. For both cases, it is proposed that it is possible to design a mesh such that the cells close to the deforming solid are "stiff" and they will convect with the deforming body. Since the largest magnetic field gradients are expected to be found at the interface of the solid and free space, it is natural that one concentrates the triangulation in this region and not in the far-field where a more uniform magnetic field is expected.

8. NUMERICAL EXAMPLES

In this section we provide numerical examples to demonstrate the capabilities of the coupled formulation, the linear solver strategy and the approach to the mesh motion problem. We focus in particular on problems in which finite deformation of a near incompressible media takes place and high electric or magnetic fields are induced. Comparison can be made between the latter two examples and the classical variational formulations presented by Bustamante [94, 95], wherein the interaction of soft polymers with rigid bodies for the electro- and magneto-elastic problems have been described.

The volumetric energy density function that is utilised in all examples is [55]

$$\Psi_0^{\text{vol}}(J) = \frac{\kappa}{4}\left[J^2 - 1 - 2\ln J\right] \quad , \tag{52}$$

where the bulk modulus is [81]

$$\kappa = \lambda + \frac{2\mu}{3} = \frac{2\mu\left[1+\nu\right]}{3\left[1-2\nu\right]} \quad . \tag{53}$$

As all presented problems are quasi-static and the materials used are hyperelastic (non-dissipative), time t reduces to a parameter that governs the applied load. For examples in which the free space is modelled, the truncated boundary has been made sufficiently far from the elastic body so have no influence on its deformation and the field permeating it. This implies that the electric/magnetic field in the vicinity of the boundary is uniform.

8.1. Pinned electroactive plate in free space

To validate the numerical implementation and highlight the general behaviour of the mesh motion algorithm, we analyse the quality of the free space mesh resulting from the electric activation of a pinned square plate. This problem has been used previously by Vu and Steinmann [38], and Vu [33] to investigate the influence of the free space on an electro-elastic body, as well as various approaches to model it. Illustrated in figure 3 is a plate of length $60 \times 60 \times 10\mu\text{m}^3$ immersed in a free space volume of dimensions $300 \times 300 \times 10\mu\text{m}^3$. The length of the plate is discretised by 20 elements, a single element through its thickness and a total of 2100 cells in the free space. A five cell thick boundary layer mesh was constructed adjacent to the plate. This coarse discretisation is neither sufficient to fully resolve the electric singularities that will develop at the plate corners nor

the constrained deformation of the plate. However, it serves to highlight aspects of the possible mesh motion strategies discussed in section 7.

The Z-orientated edges of the electroelastic plate were fully pinned ($\boldsymbol{\varphi} = \overline{\boldsymbol{\varphi}} = \mathbf{0}$). The magnitude of the prescribed potential on the upper (positive) and lower (negative) sides of the plate $\overline{\Phi} = \Phi^{\max} t$ with $t \in [0, 1]\,\mathrm{s}$ and $\Phi^{\max} = 500\,\mathrm{V}$ such that the maximum potential difference between them is $\max(\Delta\Phi) = 1000\,\mathrm{V}$. Periodic conditions between the +Z and -Z surfaces were enforced to ensure that the solution remains symmetric through its depth. This reduces the three-dimensional elastic problem to one of plane-strain. For the mesh motion problem, in addition to the continuity of the displacement at the solid-free space interface, the boundary nodes were allowed to slide along the surfaces of the reference geometry.

The isochoric component of the stored energy function is an additive decomposition of a Neo-Hookean model and a prototype coupled electro-elastic model

$$W_0\left(\overline{\mathbf{C}}, \underline{\mathbb{E}}\right) = \frac{\mu}{2}\left[\overline{\mathbf{C}} : \mathbf{I} - 3\right] + \alpha\varepsilon_0\left[\mathbf{I} : \underline{\mathbb{E}} \otimes \underline{\mathbb{E}}\right] + \beta\varepsilon_0\left[\overline{\mathbf{C}} : \underline{\mathbb{E}} \otimes \underline{\mathbb{E}}\right] + \eta\varepsilon_0\left[\overline{\mathbf{C}}^{-1} : \underline{\mathbb{E}} \otimes \underline{\mathbb{E}}\right] \quad . \tag{54}$$

The constitutive parameters, taken from [33], are $\mu = 50\,\mathrm{kPa}$, $\alpha = 0.2$, $\beta = 2$, $\eta = -2.5$. By varying the value of λ both the compressible and incompressible case are considered.

The displacement along the upper and side edges of $\partial\mathcal{B}_0$ are shown in figure 4 for several values of the potential difference. For the compressible case ($\lambda = 60\,\mathrm{kPa} \Rightarrow \nu = 0.273$) these results are qualitatively similar to those presented in [33], with the slight deviation in response to the benchmark solution being due to the difference in the utilised (isochoric) stored energy function. Due to the quadratic dependence of the energy function on the electric field, the displacement of the upper surface increases considerably as the electric load is linearly increased. Above $\Delta\Phi = 600\,\mathrm{V}$, the contraction of the upper and lower surfaces towards one another is increasingly inhibited by the displacement constraint at the plate corner.

For the nearly incompressible case ($\lambda = 249.95\,\mathrm{MPa} \Rightarrow \nu = 0.4999$), the displacement solution is very different to the compressible case. Although the displacement of the lateral edge is increased considerably at high electric fields, less vertical constriction of the body takes place. Imposition of the quasi-incompressibility condition leads to significant deformations near the pinned corners of the plate. It was observed that, for this discretisation, only the first 7 load steps can be computed when the free space mesh update is not performed. Application of a greater potential difference leads to an invalid deformation map ($\det\mathbf{F} < 0$) in a part of the free space. From this it is concluded that the use of a mesh update strategy is vital for this example that exhibits finite deformations.

8.1.1. Mesh motion study The various schemes listed in section 7 are evaluated by investigating the worst element scaled Jacobian [96] for this test case. This measure of quality was chosen as it is directly linked to the element geometry but is independent of its size. It relates to the quality of computation at the quadrature points, with value close to unity indicating excellent numerical properties and a negative value indicating an non-invertible deformation map. Shown in figure 5 is a subset of results providing a visual depiction of the updated mesh position, while table II presents the quality of the problematic cell located in the free space adjacent to the solid body and constrained vertices.

Overall the best mesh quality was produced by a single-sweep Laplace-type algorithm. Apart from this individual case, its performance with the different stiffness functions was consistently poorer than that of the elastic update methods. In general the use of elastic-type update methods reliably led to free space meshes of overall higher quality at the point of singularity at the plate corner. Increasing the parameter $\alpha \to 1$ results in the free space mesh being convected with the moving body. A large component of the grid distortion is thus propagated throughout the mesh, away from the body towards the boundary. Although this leads to better local quality at the point of interest, there is a discernible degradation of the mesh quality distant to $\mathcal{B}_0$. This impact can be controlled though the use of different stiffening functions $k(\mathbf{X})$, for which the inverse distance function with an exponent of 2 typically performed best. It is clear that utilising a distance-based stiffness parameter in association with a power function led to consistently good results. Collectively these two schemes tended to transport the free space mesh with the solid, thereby preventing the localisation of deformation to that of the problem cell. These results suggest that for this class of problems, wherein a constrained body is fully immersed in a large free space domain, a robust and reliable free space update method can be produced by using equation $(51)_2$ in conjunction with $\alpha = 0.98$.

8.1.2. Solver and convergence study To study the convergence characteristics of the compressible and incompressible problem using different solver settings, we coarsely discretise the domain (initially with 4 cells in $\mathcal{B}_0$ and 60 in $\mathcal{S}_0$, for which the mesh unit length described in $\mu\mathrm{m}$) and solve the boundary value problem for differing levels of global, isotropic h-refinement. The iterative solution scheme that we employ here is described by equation (40) with the following settings: The operation $\widetilde{\mathbf{S}}^{-1}(\bullet)_{\boldsymbol{\varphi}}$ is solved to an accuracy of three decimal places wherein the inner operation $\mathbf{K}_{\Phi\Phi}^{-1}(\bullet)_{\Phi}$ is solved to six decimal places. For this step of the process the AMG preconditioners for both $\mathbf{K}_{\boldsymbol{\varphi}\boldsymbol{\varphi}}^{-1}$ and $\mathbf{K}_{\Phi\Phi}^{-1}$ both employ a single V-cycle and have an aggregation threshold of 1×10^{-4}. The preconditioner to the Schur complement (that is the approximation to $\widetilde{\mathbf{S}}^{-1}(\bullet)_{\boldsymbol{\varphi}}$) is also solved to six decimal places and the SSOR preconditioner that approximates the inverse of $\mathbf{K}_{\Phi\Phi}^{-1}$ has an over-relaxation value of 0.7.

In figure 6 it is observed that the effectiveness of the constructed iterative solver rivals that of the direct solver. That the convergence rates are near-identical for both cases demonstrates that the chosen settings for the iterative solver preserve the accuracy of the numerical solution throughout the Newton–Raphson procedure. Although this should not be strictly necessary (as, given a reasonable initial guess, the Newton–Raphson algorithm is self-correcting), it was observed that convergence of this particular problem at high electric loads relied on the computation of an accurate solution update at each Newton step.

As is shown in figure 7, for this problem the use of the implemented iterative solution scheme leads to significantly longer linear solver times when compared to the direct solver. This may be partially attributed to the nested Schur operation and necessity to have an accurate inner solver step. However, it was observed that over the course of the last two load steps in particular the number of outer CG solver iterations required to compute the inverse Schur operation increased from approximately 5 up to 40 for the compressible case and 40 to 75 for the incompressible case. Under high electric loads, the Maxwell stress contribution becomes more dominant. As we only

compute the approximation to its tangent, the loss of accuracy in its linearisation is reflected as an increase in the stiffness of the linear system.

Table III provides a comparison of the number of Newton iterations needed at each fixed load step for different computations of the tangent. In particular, we test the cases for which we compute the exact tangent against that for which we exclude the material tangent contribution from the Maxwell stress. To mitigate any possible influence of solver error, a direct solver is used. Convergence is attained when the residual norm $|\mathbf{r}| < 1 \times 10^{-9}$.

It was observed that the exclusion of the Maxwell tangent contribution does not affect the convergence rate at relatively low electric field strength. However, using the approximate tangent leads to a significant benefit for both the compressible and incompressible cases at higher electric loads. Although the rate of convergence decreases when a fixed load step is used (reducing from quadratic towards superlinear convergence), we delay the solver divergence that occurs when the exact tangent is utilised and the positive-definite property of the global stiffness matrix is lost. It should however be noted that at higher loads than those shown here, divergence does still occur for the case of the approximate tangent as the influence of the Maxwell stress becomes dominant.

8.2. Electroactive polymer strip

In this example we broadly replicate experiments conducted on quasi-incompressible viscoelastic dielectric polymers by Hossain et al. [97]. Shown in figure 8a is the partially prestretched polymer that undergoes further mechanical loading to reach the state shown in figure 8b, and subsequent electric loading. In order to apply a potential difference to the specimen's surface, a conductive material has been applied to the face of the sample with a small strip at the edge of the face left unpainted. Figure 8c depicts the reference geometry for this problem, with the material domain being reduced to a $\frac{1}{8}$ model due to symmetry conditions. The reduced domain has dimensions $(17.5 + 2.5) \times 5 \times 0.5 \ \mathrm{mm}^3$ and is discretised by $(30 + 10) \times 25 \times 8$ low-order finite elements. There is a concentration of elements towards the line separating the conductive and non-conductive areas on the front face, as it is expected that a large lateral potential gradient will be generated in this region. The number of degrees-of-freedom for each field in the coupled problem are $\left\{\boldsymbol{\varphi}, \widetilde{p}, \widetilde{J}, \Phi\right\} = \{28782, 8000, 8000, 9594\}$.

The boundary conditions for the reduced problem are as follows: Due to the geometric symmetry, constrained planar motion is prescribed on the X-,Y- and Z- (symmetry) planes and a zero electric potential condition is enforced on the X-Y plane. A time-dependent deformation on the +Y face is prescribed in order to represent the two stages of prestretching before the potential difference is applied[7]. On this surface, we ensure that

$$\overline{\varphi}_2\left(\mathbf{X}\right) = \begin{cases} \dfrac{t}{30}(\lambda_2 - 1)\, X_2 & \text{if} \quad t \leq 30\,\mathrm{s} \\ (\lambda_2 - 1)\, X_2 & \text{otherwise} \end{cases} \tag{55}$$

[7]In order to minimise mesh distortion, lateral and vertical prestretch is performed in the opposite order to that in which it is conducted in experiments. However, as the chosen constitutive model is hyperelastic the deformation due to the electric loading is independent of the stress history.

$$\overline{\varphi}_1\left(\mathbf{X}\right) = \begin{cases} X_1 & \text{if} \quad t \leq 30\,\mathrm{s} \\ \dfrac{t-30}{30}\left(\lambda_1 - 1\right) X_1 & \text{if} \quad 30\,\mathrm{s} < t \leq 60\,\mathrm{s} \\ \left(\lambda_1 - 1\right) X_1 & \text{otherwise} \end{cases} \tag{56}$$

for which the stretches are $\lambda_1 = 3$, $\lambda_2 = 5$ and $t \in [0, 120]\,\mathrm{s}$. On the +Z face for which $0 \leq X_1 \leq 17.5$, the applied electric potential is

$$\overline{\Phi} = \begin{cases} 0 & \text{if} \quad t \leq 60\,\mathrm{s} \\ \dfrac{t-60}{60}\,\Phi^{\max} & \text{otherwise} \end{cases} \tag{57}$$

with $\Phi^{\max} = 5000\,\mathrm{V}$. The remaining surfaces remain mechanically and electrically traction free.

Although some characterisation of this EAP material has been performed [98, 23, 97], for the purpose of demonstration we will assume a hyperelastic constitutive law with a simplified coupled component. The stored energy function W_0 is additively decomposed into mechanical and electro-aelectro-active components. The Arruda–Boyce 8-chain model [99] is used to represent the elastic part and a prototype function [20] for the electro-active component

$$\begin{aligned} W_0\left(\overline{\mathbf{C}}, \underline{\mathbb{E}}\right) = \frac{\mu}{K}\sum_{i=1}^{5}\gamma_i\,\omega^{(i-1)}\left[\left[\overline{\mathbf{C}} : \mathbf{I}\right]^i - 3^i\right] \\ + \alpha\varepsilon_0\left[\mathbf{I} : \underline{\mathbb{E}} \otimes \underline{\mathbb{E}}\right] + \beta\varepsilon_0\left[\overline{\mathbf{C}} : \underline{\mathbb{E}} \otimes \underline{\mathbb{E}}\right] + \eta\varepsilon_0\left[\overline{\mathbf{C}}^{-1} : \underline{\mathbb{E}} \otimes \underline{\mathbb{E}}\right] \quad , \end{aligned} \tag{58}$$

where

$$\omega = \frac{1}{N} \quad , \quad K = \left[1 + \frac{3}{5}\omega + \frac{99}{175}\omega^2 + \frac{513}{875}\omega^3 + \frac{42039}{67375}\omega^4\right] \quad , \tag{59a}$$

$$\gamma_1 = \frac{1}{2} \quad , \quad \gamma_2 = \frac{1}{20} \quad , \quad \gamma_3 = \frac{11}{1050} \quad , \quad \gamma_4 = \frac{19}{7000} \quad , \quad \gamma_5 = \frac{519}{673750} \quad . \tag{59b}$$

The chosen elastic constitutive parameters $\mu = 13.5\,\mathrm{kPa}$, $N = 784 \times 10^3$ were taken from [23], the Poisson ratio $\nu = 0.4999$ and the electro-mechanical parameters[8] were $\alpha = 50$, $\beta = 10 \times 10^3$, $\eta = -37.5 \times 10^{-3}$. The respectively large and small values for β and η are appropriate as the stretch in the thickness direction $\lambda_3 \ll 1$ and the large electric field is aligned with $\mathbf{e}_3$.

Illustration to the extent of deformation applied during the mechanical loading phase is given in figure 9. With the application of equations (55) and (56) the material is initially deformed vertically by $400\,\%$ after which the upper surface is extended laterally by $200\,\%$.

As is observed in figure 10, the geometry changes further upon application of the potential difference across the surface of the polymer. The central region of strip (along the centreline $\mathbf{C} - \mathbf{B} - \mathbf{A}$ shown in figure 8c) expands outwards as the conductive surfaces contract towards each other. As the assumed energy function is quadratic in $|\underline{\mathbb{E}}|$, a very high electric field is required to induce large displacements in the media. As expected, in the central region there exists a potential gradient aligned through the thickness of the material. Furthermore, due to the lack of a conductive

[8]These parameters were chosen such that application of $10\,\mathrm{kV}$ leads approximately $10\,\%$ additional lateral deformation of the prestretched material. This loosely correlates to the displacement observed during experimental analysis of this material under similar conditions.

material at the sample edge (and the chosen constitutive model), the potential field in this region is non-uniform, with the edge experiencing a low voltage.

Figure 11a shows the displacement history for the point **A** at the intersection between the traction-free surfaces and the X-Z plane. The thickness of the material (as computed from the Z-displacement) decreases non-linearly here throughout the course of the applied load, with the largest change occurring during the first phase of stretching. After mechanical and electric loading the free perimeter is slightly less than $20\,\%$ of its original thickness. During the initial phase of stretching, the sample contracts laterally but then expands significantly as lateral stretch at the gripped surface is prescribed. This expansion continues in a non-linear manner as the surface potential is increased. Application of the voltage difference results in the pre-stretched spatial position of point **A** moving from $x \approx 49.1\,\mathrm{mm}$ to $x \approx 53.6\,\mathrm{mm}$. This equates to an overall increase in lateral stretch of approximately $9.2\,\%$ which corresponds to the deformation typically observed in experiments conducted under similar conditions. This response is primarily due to the near-incompressibility of the material and imposed boundary conditions, as after the prestretch phase any reduction in thickness must correspond to a lateral expansion along the midline.

Plotting the displacement along the midline of the surface of the applied potential reveals that the sample thickness is not constant, primarily due to the spatially non-uniform loading conditions. As is shown in figure 11b, the central region of the material is always compressed to a greater extent than the perimeter, with the difference becoming more pronounced as the prescribed mechanical deformation increases. The central region of the $\frac{1}{8}$ geometry is approximately $25\,\mu\mathrm{m}$ thick after both mechanical loading steps, which is four times less than at the perimeter. Upon application of the electrical load, the thickness at position **C** does not change significantly. Compression of the material is rather observed mainly in the vicinity of **B**, towards the edge of the painted region. At this point the full electric load reduces the thickness by approximately $37\,\%$ and leads to a sharp transition in the measured deformation between the region under the direct influence of the applied load and that with no conductive material on the surface near it. After all loading is applied, the thickness profile in the central region is ultimately three times less than that of the perimeter.

Presented in figure 12 is the lateral and vertical true stress history recorded at the quadrature point closest to the origin (the geometric centre of the full geometry) and point **A** at the boundary. At both measurement points the mechanical loading results in an increase in stress in the respective directions, with the maximum stress in the Y-direction being 1 order of magnitude larger than that in the X-direction at **O**, and 3 orders of magnitude larger at **A**. Application of the electric load induces stress softening at **O** in both coordinate directions. At the boundary however there is no appreciable change in the vertical component of the stress tensor and σ_{XX} appears to decrease asymptotically as the material expands laterally.

Measuring the overall dilatation as the change in material volume

$$\theta = \frac{\mathrm{V}_t}{\mathrm{V}_0} = \int_{\mathcal{B}_0} J \Big/ \int_{\mathcal{B}_0} 1 \quad , \tag{60}$$

it was observed the weakly imposed quasi-incompressibility of the polymer was maintained throughout the simulation as the maximum relative dilatation given by $\theta - 1$ was $0.59\,\%$. For this example with the mixed formulation, load steps of size $0.5\,\mathrm{s}$ were required for stable displacement loading for which the linearised problem was solved using equation (44) (an inexact linear

increment). As a point of comparison, the same problem was repeated using a standard $Q2-Q2$ ansatz for the displacement and potential fields. The grid was coarsened such that the total number of $\{\boldsymbol{\varphi}, \Phi\}$ degrees of freedom in each grid direction were similar to the previous example. Although a direct solver was utilised (thereby producing an "exact" linear increment), a load step size of $0.05\,\mathrm{s}$ (10 times smaller) was necessary to achieve convergence during the mechanical loading stage. Furthermore, stability issues (not present for the mixed formulation) were noted at very high electric fields.

As confirmation of the lack of influence of the ponderomotive force in the functioning of condensator-like geometries, the same problem was repeated with the free space, clamps (of which it is assumed all four comprise undeformable steel for which the constitutive parameters were assumed to be $\alpha = 0$, $\beta = 0$, $\eta = -5 \times 10^5$), and polymeric material gripped by the clamps included. To attain the correct deformation state the displacement conditions given by equations (55) and (56) were prescribed to the clamped material. To attain the correct spatial configuration during the prestretch phase of loading, the (artificial) motion of various parts of the free space geometry were prescribed as well. The part of the clamp that was in contact with the material was also made to stretch at an equal rate to the polymer. The region of the domain both above and to the side of the polymer was allowed to translate with the deforming body. For the final configuration to be representative of the state shown in figure 8b, it was therefore required to compute a suitable reference domain $\overline{\mathcal{B}_0 \cup \mathcal{S}_0}$ that would transform to the correct spatial configuration $\overline{\mathcal{B}_t \cup \mathcal{S}_t}$ under these conditions. The deformation of the free space was performed using an elastic update approach with $\alpha = -0.1$, while the stiffness parameter was set using the vertex distance approach with $p = 1.25$. To prevent excessive grid distortion, the mesh motion at and above the height of the clamp was fully prescribed, as was the Z-displacement of the mesh below it. Therefore only movement in the X-Y plane in front and alongside the cross-section of material was computed.

Presented in figure 13 is the spatial configuration of the problem after the mechanical loading steps have taken place and its state after the electric loading has also been applied. Due to the symmetry condition, a strong electric field was present in the gap above the sample, but as the material is fixed in the metallic clamp it did not influence the displacement result. However, as can be expected, the electric field generated in the clamp and rest of the free space surrounding the sample is negligible and therefore the displacement and potential solution in the region of interest are not significantly affected. This, therefore, confirms that only the reduced geometry illustrated in figure 8 need be considered for problems of this nature.

8.3. Magnetoactive polymer valve

Finally, we examine a simplified magneto-active valve that broadly replicates the coil-activated design presented by Böse et al. [2, figure 2]. Figure 14 illustrates the truncated geometry of the valve, with the magneto-active polymer denoted as $\mathcal{B}_0$, and the iron inner yoke and casing by $\mathcal{S}_0^{I,i}$ and $\mathcal{S}_0^{I,o}$ respectively. The magnetisable polymer was considered deformable, while the very stiff iron components were fully immobile (and therefore not represented as an elastic solid). The height and radius of the inner yoke are $9\,\mathrm{mm}$ and $3\,\mathrm{mm}$ respectively, while the casing has a height of $7\,\mathrm{mm}$, an inner radius of $14\,\mathrm{mm}$ and outer radius of $18\,\mathrm{mm}$. The outer radius of the polymer is $12\,\mathrm{mm}$ and its overall thickness is $5\,\mathrm{mm}$. The initial gap between the polymer and casing was therefore $2\,\mathrm{mm}$. The free corners of the polymer were rounded with a fillet of radius $0.25\,\mathrm{mm}$ to prevent the generation

of magnetic singularities along these edges. However, sharp corners of the iron components were retained. The height and radius of the truncated far-field $\mathcal{S}_0$ were, respectively, $24\,\mathrm{mm}$ and $33\,\mathrm{mm}$. Although the problem is axisymmetric, one quarter of the full 3-d model is represented.

A combination of structured and unstructured mesh techniques were used to discretise the complex geometry. Within a radius of $0.25\,\mathrm{mm}$ of the three sharp corners marked $\mathbf{R}$ in figure 14, three levels of local h-refinement were manually performed in order to capture the magnetic singularity that was expected to develop in these locations. A fine mesh was used in the region surrounding the polymer in order to capture the sharp change in the magnetic field through the different media. After refinement, a total of $103\,283$ computational cells were present. The overall number of degrees-of-freedom in the primary problem were $\left\{\boldsymbol{\varphi}, \widetilde{p}, \widetilde{J}, \Phi\right\} = \{20\,412, 4832, 4832, 119\,223\}$, while the ancillary mesh-motion problem required $\{\boldsymbol{\varphi}\} = \{342\,657\}$ degrees-of-freedom. The iterative solver scheme outlined in equation (40) was utilised in the solution of the linearised problem.

As the magnetic scalar potential formulation is utilised, the coil cannot be directly represented. However, an approximation of its effect is instead captured through the applied potential boundary conditions. A magnetic potential is prescribed at the surface of truncation of the casing and inner yoke, with the casing set to have zero potential and that at the inner yoke

$$\overline{\Phi} = \sqrt{t}\Phi^{\max} \tag{61}$$

with $t \in [0, 1]$ and $\Phi^{\max} = 310\,\mathrm{A}$. The elastic body is constrained only at the interface between it and the inner yoke. Here we prescribe that the central displacement degrees-of-freedom remain fixed in space, while the rest of the surface can slide freely along the interface. With respect to the mesh update problem, we allow the mesh in free space to slide along "solid" geometries, namely the outer casing and iron yoke, as well as along $\partial\mathcal{S}_0$ (the boundary of the free space at the edge of the computational domain).

An additively decomposed Neo-Hookean model and a prototype coupled magneto-elastic model

$$W_0\left(\overline{\mathbf{C}}, \underline{\mathbb{H}}\right) = \frac{\mu}{2}\left[\overline{\mathbf{C}} : \mathbf{I} - 3\right] + \alpha\mu_0\left[\mathbf{I} : \underline{\mathbb{H}} \otimes \underline{\mathbb{H}}\right] + \beta\mu_0\left[\overline{\mathbf{C}} : \underline{\mathbb{H}} \otimes \underline{\mathbb{H}}\right] + \eta\mu_0\left[\overline{\mathbf{C}}^{-1} : \underline{\mathbb{H}} \otimes \underline{\mathbb{H}}\right] \tag{62}$$

with constitutive parameters $\mu = 30\,\mathrm{kPa}$, $\alpha = -0.5$, $\beta = -4$, $\eta = -0.5$ were used for the isochoric component of the polymer energy density function. In the small strain regime, this corresponds to a relative magnetic permeability $\mu_\mathrm{r} \approx 10$. This is somewhat greater than that typically measured in magneto-active polymers [100] but necessary to induce large displacements in this example problem. The material was made quasi-incompressible by choosing $\nu = 0.4999$. The total stored energy function for the (inelastic) iron components was

$$\Psi\left(J, \mathbf{C}, \underline{\mathbb{H}}\right) = \mu_\mathrm{r} M_0\left(J, \mathbf{C}, \underline{\mathbb{H}}\right) \tag{63}$$

with the relative magnetic permeability $\mu_\mathrm{r} = 5000$.

The imposed set of magnetic boundary conditions effectively produces a qualitatively similar magnetic induction field to that observed when the curl-formulation for the magnetic problem, which can directly represent rotational magnetic fields induced by currents, is used. To demonstrate that this is indeed the case, figure 15a illustrates the magnetic field generated when directly

modelling the coil using the vector potential formulation (with no consideration of elastic deformation). Comparing this result to that obtained using the truncated domain and scalar potential formulation, we observe that the magnetic field is both qualitatively and quantitatively similar. The domain truncation in $\mathcal{S}_0^l$ forces the component of the magnetic field normal to the boundary to vanish; a numerical artefact that is not seen in the vector potential formulation. This error could be partially mitigated though the use of the traction boundary condition listed in equation $(25\text{d})_2$, but is not considered in this demonstration problem.

The spatial magnetic field and induction measured along the midplane of the polymer is presented in figure 16a. This result is qualitatively similar to that shown by Böse et al. [2] for a static geometry with matching characteristics. While the magnetic field strength is very low in the iron yoke and casing, it is larger in the less permeable materials with the highest value recorded within the free space adjacent to the polymer. The field strength in the gap and polymer decrease non-linearly as the radius increases due to the non-linear material constitutive law and deformation. It should be noted that the jump in the magnetic field strength at the polymer-air interface $\overline{\mathcal{B}_0} \cap \overline{\mathcal{S}_0^g}$ gets disproportionally larger with increasing load step. Due to its proximity to the source of the potential the magnetic induction in the inner yoke is very large. Within the polymer it decays non-linearly from the inner to the outer radius in response to the non-linear magnetic field. By comparison, the induction within the gap appears almost constant for a given magnetic load.

In figure 17 we plot both the radial and axial displacement along the polymer midplane. For the specified geometry and constitutive models, at the maximum loading conditions the gap radius was reduced by $25\,\%$[9]. Due to the influence of the ponderomotive force and, to a lesser extent, the material non-linearity the radial displacement was not directly proportional to $\sqrt{t}$ (as might be expected since the energy function is quadratic in $|\underline{\mathbb{H}}|$). The ponderomotive force is driven by the jump in the magnetic field at the interface, and therefore the large radial gradient in the magnetic field at the surface $\overline{\mathcal{B}_0} \cap \overline{\mathcal{S}_0^g}$ produces a large traction here. As measured by a small negative axial displacement along its radius, the asymmetry of the magnetic field above and below the polymer led to it bending slightly downwards. However, as is suggested the comparison given in figure 15, the phenomenon may be a result of, or at least exacerbated by, the truncation of the domain below the polymer. With reference to the material dilatation (equation (60)), the volume change after application of the full magnetic load was less than $0.0032\,\%$.

To further highlight the role of the ponderomotive force in the functioning of this design (specifically using an isotropic magneto-elastic polymer with a large relative permeability), we compare the maximal displacement configuration of the polymer as computed with and without the surrounding free space. Accounting for the free space, we observe a relatively large overall deformation of the material, along with an asymmetric axial displacement due to the non-uniform magnetic field. Furthermore, although the surface $\overline{\mathcal{B}_0} \cap \overline{\mathcal{S}_0^g}$ is attracted towards the outer casing $\mathcal{S}_0^{I,o}$ (thereby reducing the material thickness), there exists a large magnetic field in the vicinity of the filleted corners that leads to an axial ponderomotive force acting on the polymer. The net result is that the thickness of the material here is greater than at its inner radius and the surface becomes slightly concave. In contrast, when inducing a similar field within the media without accounting

[9] Higher magnetic fields could not be evaluated due to well understood numerical issues related to the tangent contribution derived from the Maxwell stress. Therefore no further deformation could be induced without compromising the numerical stability of the problem.

for the surrounding free space, only relatively small displacements are produced and the axial displacement field is symmetric about the midplane. This difference could potentially be corrected by adding a representative traction condition to the second case. However, this would require an *a priori* knowledge of surrounding magnetic field.

The mesh motion analysis presented in section 8.1 suggests that several combinations of settings for equation (50) may lead to satisfactory results for the solution of the free space deformation map. Here we make a note of the difference in the updated mesh resulting from the method ultimately chosen for this purpose ($\alpha = -1$ with a vertex-distance stiffness function and power law with $p = 1.25$) and the anticipated next best strategy ($\alpha = 0.98$ with a vertex-distance stiffness function and power law with $p = 2$). To perform the free space mesh update for this problem, we allowed the mesh to slide along "pseudo-solid" geometries, namely the outer casing and iron core, as well as along $\partial\mathcal{S}_0$ (the boundary of the free space at the edge of the computational domain). Furthermore, the vertex positions of the "pseudo-solid" media (namely $\partial\mathcal{S}_0^{I,i}$ and $\partial\mathcal{S}_0^{I,o}$, which were not endowed with elastic degrees-of-freedom in the coupled problem) were also considered when defining the effective stiffness of the free space.

Figure 19 illustrates the deformation map resulting from these two strategies at maximum magnetic load. Of specific importance is the deformation within the gap $\mathcal{S}_0^g$, highlighted in red. Using a Laplace-type update strategy, there is a controlled reduction in the volume of the gap that leads to minimal distortion of the mesh in this region, as well as around it. However, as is highlighted in figure 19b, the elasticity-based approach to the update resulted in significant distortion as the material is "squeezed" out of the gap. It is anticipated that the latter method would be unsustainable at higher deformations while the former could accommodate it.

Figure 20 illustrates the functioning and performance of the valve when the polymer is attached to the outer casing and expands inwards under the application of the magnetic field. Due to limitations in the model stemming from the new geometry the pinned boundary condition was moved from the centreline of the polymer to the upper edge coinciding with $\mathbf{R}_2$. For the magneto-elastic case the maximum applied potential was lowered to $\Phi^{\max} = 243\,\mathrm{A}$ due to numerical stability issues.

Comparing figure 20a to figure 15b we observe that, for the same applied potential, the magnetic field strength in the gap is significantly greater and material magnetisation has been decreased. This is confirmed in the magneto-elastic case for which the magnetic field and induction strength at the polymer midline and are shown in figure 20c and figure 20d respectively. We note that for this second geometry the applied potential at $t = 1$ is nearly equivalent to that for the first at $t = 0.7$. It is observed that the jump in the magnetic field at the radial polymer-free space interface is significantly larger than before, implying that the ponderomotive traction is stronger for this geometry. However, the maximum radial displacement is comparable for the two geometries at similar applied potentials, although this result may be influenced by the imposed displacement boundary conditions.

9. DISCUSSION AND CONCLUSIONS

A mixed variational formulation for quasi-incompressible electro- or magneto-active polymers, which accounts for the influence of the surrounding free space, has been presented. We have demonstrated a novel domain decomposition that can be leveraged to separate the primary coupled

problem and secondary mesh update problem for the free space. Thus we were able to select independent and most-suitable approaches to solving the multiphysics and artificial mesh motion problems, resulting in the smallest possible linear problem for the given discretisation. This is particularly advantageous due to the arbitrary motion of the deformation map in the free space. Iterative solution strategies for the linearised problem that exploit its block substructure were also presented and discussed.

Overall, the mixed formulation and solution strategy were shown to be robust for several example problems that are applicable to research in the field of electro- and magneto-elasticity. All of these involved near incompressible media, large deformations and high electro-magnetic loadings. It was shown therein that the near incompressibility condition was successfully imposed. We presented a detailed discussion on their implementation and solution procedure, and highlighted some of the fundamental behaviours of these geometries. Using an approximation for the tangent of the Maxwell stress contribution was shown to be beneficial at high electro-magnetic loads, delaying the occurrence of divergence in the nonlinear solver with no apparent loss in convergence rate at low loads. It was found that for one tested geometry the use of a direct solver, as opposed to an iterative one, for the linear problem was the superior choice. This is because high deformation and electro-magnetic loads, the loss of accuracy for the linearisation of the Maxwell stress contribution becomes more significant. A comparison was also conducted on the solutions of the problems with and without the inclusion of free space, thereby empirically demonstrating when it need be considered.

We illustrated the functioning of the general, elasticity-based free space mesh update method using several test cases. A three parameter constitutive model was developed to adapt the nature of the update algorithm based on various physical and geometric parameters. From the analysis of the numerical example problems we were able to demonstrate how several update strategies influence the displacement map in the free space. From this we provided insight as to how parameter choices affect its functioning and which might be more applicable for particular geometries. This approach was easy to implement and easy to control for relatively small but finite deformations, for which both the Laplace and elasticity-based approaches can be made to work sufficiently well. However, for problems involving very large deformations or highly constrained movement of solid bodies the disadvantages of physically based update algorithms became apparent. More guided control over the mesh movement was necessary, indicating that quality-based update methods may be most suitable for these applications.

ACKNOWLEDGEMENTS

The support of this work by the European Research Council (ERC) through the Advanced Grant 289049 MOCOPOLY is gratefully acknowledged by the authors. The authors would like to thank Dr. M. Hossain for the conversations surrounding the example problem given in section 8.2 and for supplying the photographs shown in figure 8.

A. LINEARISATION OF COUPLED PROBLEM

From equation (24), the first-order Taylor expansion of the residual is

$$0 \equiv \delta\Pi\Big|_{\boldsymbol{\varphi},\widetilde{p},J\Phi} + \Big[\mathrm{D}_{\Delta\boldsymbol{\varphi},\delta\boldsymbol{\varphi}}\Pi^{\text{int}} + \mathrm{D}_{\Delta\widetilde{J},\delta\widetilde{J}}\Pi^{\text{int}} + \mathrm{D}_{\Delta\widetilde{J},\delta\widetilde{J}}\Pi^{\text{int}} + \mathrm{D}_{\Delta\Phi,\delta\Phi}\Pi^{\text{int}}\Big] \tag{64}$$

for which the resulting direct terms of the linearisation (assuming a dead load) are

$$\begin{aligned}\mathrm{D}_{\Delta\boldsymbol{\varphi},\delta\boldsymbol{\varphi}}\Pi^{\text{int}} = &\int_{\mathcal{S}_0} \Delta\delta\mathbf{E} : \mathbf{S}^{\max}\, dV + \int_{\mathcal{S}_0} \delta\mathbf{E} : \boldsymbol{\mathcal{H}}^{\max} : \Delta\mathbf{E}\, dV + \int_{\mathcal{B}_0} \Delta\delta\mathbf{E} : \left[\overline{\mathbf{S}}^{\text{tot}} + \widetilde{p}J\mathbf{C}^{-1}\right] dV \\ &+ \int_{\mathcal{B}_0} \delta\mathbf{E} : \left[\overline{\boldsymbol{\mathcal{H}}}^{\text{tot}} + \widetilde{p}J\left[\mathbf{C}^{-1}\otimes\mathbf{C}^{-1} - 2\mathbf{C}^{-1}\overline{\otimes}\mathbf{C}^{-1}\right]\right] : \Delta\mathbf{E}\, dV \quad ,\end{aligned} \tag{65a}$$

$$\mathrm{D}_{\Delta\widetilde{J},\delta\widetilde{J}}\Pi^{\text{int}} = \int_{\mathcal{B}_0} \delta\widetilde{J}\left[\frac{\partial^2\Psi_0^{\text{vol}}}{\partial\widetilde{J}^2} + \frac{\partial^2 W_0}{\partial\widetilde{J}^2}\right]\Delta\widetilde{J}\, dV \quad , \tag{65b}$$

$$\mathrm{D}_{\Delta\Phi,\delta\Phi}\Pi^{\text{int}} = -\int_{\mathcal{B}_0} \delta\underline{\mathbb{H}}\cdot\mathbf{D}^{\text{tot}}\cdot\Delta\underline{\mathbb{H}}\, dV - \int_{\mathcal{S}_0} \delta\underline{\mathbb{H}}\cdot\mathbf{D}^{\max}\cdot\Delta\underline{\mathbb{H}}\, dV \quad , \tag{65c}$$

where

$$\Delta\delta\mathbf{E} = \mathrm{sym}\left[\Delta\mathbf{F}^T\cdot\delta\mathbf{F}\right] \quad , \tag{66}$$

while the coupling terms arising from the linearisation are

$$\mathrm{D}_{\Delta\widetilde{p},\delta\boldsymbol{\varphi}}\Pi^{\text{int}} = \int_{\mathcal{B}_0} \delta\mathbf{E} : J\mathbf{C}^{-1}\,\Delta\widetilde{p}\, dV \quad , \quad \mathrm{D}_{\Delta\boldsymbol{\varphi},\delta\widetilde{p}}\Pi^{\text{int}} = \int_{\mathcal{B}_0} \delta\widetilde{p}\, J\mathbf{C}^{-1} : \Delta\mathbf{E}\, dV \quad , \tag{67a}$$

$$\mathrm{D}_{\Delta\widetilde{J},\delta\boldsymbol{\varphi}}\Pi^{\text{int}} = \int_{\mathcal{B}_0} \delta\mathbf{E} : \mathbf{R}^{\text{tot}}\,\Delta\widetilde{J}\, dV \quad , \quad \mathrm{D}_{\Delta\boldsymbol{\varphi},\delta\widetilde{J}}\Pi^{\text{int}} = \int_{\mathcal{B}_0} \delta\widetilde{J} : \mathbf{R}^{\text{tot}}\,\Delta\mathbf{E}\, dV \quad , \tag{67b}$$

$$\begin{aligned}\mathrm{D}_{\Delta\Phi,\delta\boldsymbol{\varphi}}\Pi^{\text{int}} &= -\int_{\mathcal{S}_0} \delta\mathbf{E} : \boldsymbol{P}^{\max}\cdot\Delta\underline{\mathbb{H}}\, dV - \int_{\mathcal{B}_0} \delta\mathbf{E} : \boldsymbol{P}^{\text{tot}}\cdot\Delta\underline{\mathbb{H}}\, dV \quad , \\ \mathrm{D}_{\Delta\boldsymbol{\varphi},\delta\Phi}\Pi^{\text{int}} &= -\int_{\mathcal{S}_0} \delta\underline{\mathbb{H}}\cdot\left[\boldsymbol{P}^{\max}\right]^T : \Delta\mathbf{E}\, dV - \int_{\mathcal{B}_0} \delta\underline{\mathbb{H}}\cdot\left[\boldsymbol{P}^{\text{tot}}\right]^T : \Delta\mathbf{E}\, dV \quad ,\end{aligned} \tag{67c}$$

$$\mathrm{D}_{\Delta\widetilde{J},\delta\widetilde{p}}\Pi^{\text{int}} = -\int_{\mathcal{B}_0} \delta\widetilde{p}\,\Delta\widetilde{J}\, dV \quad , \quad \mathrm{D}_{\Delta\widetilde{p},\delta\widetilde{J}}\Pi^{\text{int}} = -\int_{\mathcal{B}_0} \delta\widetilde{J}\,\Delta\widetilde{p}\, dV \quad , \tag{67d}$$

$$\mathrm{D}_{\Delta\Phi\delta\widetilde{J}}\Pi^{\text{int}} = -\int_{\mathcal{B}_0} \delta\widetilde{J}\,\mathbb{Q}^{\text{tot}}\cdot\Delta\underline{\mathbb{H}}\, dV \quad , \quad \mathrm{D}_{\Delta\widetilde{J},\delta\Phi}\Pi^{\text{int}} = -\int_{\mathcal{B}_0} \delta\underline{\mathbb{H}}\cdot\mathbb{Q}^{\text{tot}}\,\Delta\widetilde{J}\, dV \quad . \tag{67e}$$

The elastic tangent $\boldsymbol{\mathcal{H}}$, the piezo- or magneto-elasticity tensor $\boldsymbol{P}$ and the dielectricity or magnetostatic tensor $\mathbf{D}$ and ancilliary coupling tensor $\mathbf{R}^{\text{tot}}$ and vector $\mathbb{Q}^{\text{tot}}$ are defined as

$$\overline{\boldsymbol{\mathcal{H}}}^{\text{tot}} = 2\frac{\partial \overline{\mathbf{S}}^{\text{tot}}}{\partial \mathbf{C}} = 2\frac{\partial \overline{\boldsymbol{\mathcal{P}}}}{\partial \mathbf{C}} \vdots \left[2\frac{\partial W_0}{\partial \overline{\mathbf{C}}}\right] + \overline{\boldsymbol{\mathcal{P}}} : \left[4\frac{\partial^2 W_0}{\partial \overline{\mathbf{C}} \otimes \partial \overline{\mathbf{C}}}\right] : \overline{\boldsymbol{\mathcal{P}}} \quad , \tag{68a}$$

$$\mathbf{R}^{\text{tot}} = \frac{\partial \mathbf{S}^{\text{tot}}}{\partial \widetilde{J}} = \overline{\boldsymbol{\mathcal{P}}} : \left[2\frac{\partial^2 W_0}{\partial \widetilde{J} \partial \overline{\mathbf{C}}}\right] \quad , \tag{68b}$$

$$\mathbf{D}^{\text{tot}} = \frac{\partial \underline{\mathbb{B}}^{\text{tot}}}{\partial \underline{\mathbb{H}}} = -\frac{\partial^2 W_0}{\partial \underline{\mathbb{H}} \otimes \partial \underline{\mathbb{H}}} \quad , \quad \mathbb{Q}^{\text{tot}} = \frac{\partial \underline{\mathbb{B}}^{\text{tot}}}{\partial \widetilde{J}} = -\frac{\partial^2 W_0}{\partial \underline{\mathbb{H}} \partial \widetilde{J}} \quad , \tag{68c}$$

$$\boldsymbol{P}^{\text{tot}} = -\frac{\partial \mathbf{S}^{\text{tot}}}{\partial \underline{\mathbb{H}}} = \overline{\boldsymbol{\mathcal{P}}} : \left[-2\frac{\partial^2 W_0}{\partial \underline{\mathbb{H}} \otimes \partial \overline{\mathbf{C}}}\right] \quad , \quad \left[\boldsymbol{P}^{\text{tot}}\right]^T = 2\frac{\partial \underline{\mathbb{B}}^{\text{tot}}}{\partial \mathbf{C}} = \left[-2\frac{\partial^2 W_0}{\partial \overline{\mathbf{C}} \otimes \partial \underline{\mathbb{H}}}\right] : \overline{\boldsymbol{\mathcal{P}}} \quad , \tag{68d}$$

and their Maxwell counterparts in the free space are

$$\boldsymbol{\mathcal{H}}^{\text{max}} = 2\frac{\partial \mathbf{S}^{\text{max}}}{\partial \mathbf{C}} = 4\frac{\partial^2 M_0}{\partial \mathbf{C} \otimes \partial \mathbf{C}} \quad , \quad \mathbf{D}^{\text{max}} = \frac{\partial \underline{\mathbb{B}}^{\text{max}}}{\partial \underline{\mathbb{H}}} = -\frac{\partial^2 M_0}{\partial \underline{\mathbb{H}} \otimes \partial \underline{\mathbb{H}}} \tag{69a}$$

$$\boldsymbol{P}^{\text{max}} = -\frac{\partial \mathbf{S}^{\text{max}}}{\partial \underline{\mathbb{H}}} = -2\frac{\partial^2 M_0}{\partial \underline{\mathbb{H}} \otimes \partial \mathbf{C}} \quad , \quad \left[\boldsymbol{P}^{\text{max}}\right]^T = 2\frac{\partial \underline{\mathbb{B}}^{\text{max}}}{\partial \mathbf{C}} = -2\frac{\partial^2 M_0}{\partial \mathbf{C} \otimes \partial \underline{\mathbb{H}}} \quad . \tag{69b}$$

B. DETAILS OF SOLUTION OF LINEAR ITERATION STEP

Subsequent to introducing the assumption regarding the form of the energy stored in the magnetic field inside the near-incompressible body (as given in equation (39)), the amended discrete form of the linear system is

$$\begin{bmatrix} \mathbf{K}_{\boldsymbol{\varphi}\boldsymbol{\varphi}} & \mathbf{K}_{\boldsymbol{\varphi}\widetilde{p}} & \mathbf{0} & \mathbf{K}_{\boldsymbol{\varphi}\Phi} \\ \mathbf{K}_{\widetilde{p}\boldsymbol{\varphi}} & \mathbf{0} & \mathbf{K}_{\widetilde{p}\widetilde{J}} & \mathbf{0} \\ \mathbf{0} & \mathbf{K}_{\widetilde{J}\widetilde{p}} & \mathbf{K}_{\widetilde{J}\widetilde{J}} & \mathbf{0} \\ \mathbf{K}_{\Phi\boldsymbol{\varphi}} & \mathbf{0} & \mathbf{0} & \mathbf{K}_{\Phi\Phi} \end{bmatrix} \begin{bmatrix} \Delta\mathbf{d}_{\boldsymbol{\varphi}} \\ \Delta\mathbf{d}_{\widetilde{p}} \\ \Delta\mathbf{d}_{\widetilde{J}} \\ \Delta\mathbf{d}_{\Phi} \end{bmatrix} = \begin{bmatrix} \mathbf{f}_{\boldsymbol{\varphi}} \\ \mathbf{f}_{\widetilde{p}} \\ \mathbf{f}_{\widetilde{J}} \\ \mathbf{f}_{\Phi} \end{bmatrix} \quad . \tag{70}$$

We note that $\mathbf{K}_{\widetilde{J}\widetilde{J}}$ is block diagonal due to the discontinuous nature of the dilatation field, and $\mathbf{K}_{\widetilde{p}\widetilde{J}}$, $\mathbf{K}_{\widetilde{J}\widetilde{p}}$ are uncoupled on an element level and square (and thus invertible) due to the identical choice of ansatz for $\widetilde{p}$ and $\widetilde{J}$. One may further exploit the discontinuous fields $\widetilde{p}$, $\widetilde{J}$ and perform static condensation to remove these degrees-of-freedom from the global system. From equation (70) the update of the dilatation can be expressed as equation (42) while condensation of pressure response results from equation (43). The outcome of condensing these fields into row 1 of equation (70) is

$$\begin{bmatrix} \widetilde{\mathbf{K}}_{\boldsymbol{\varphi}\boldsymbol{\varphi}} & \mathbf{K}_{\boldsymbol{\varphi}\Phi} \\ \mathbf{K}_{\Phi\boldsymbol{\varphi}} & \mathbf{K}_{\Phi\Phi} \end{bmatrix} \begin{bmatrix} \Delta\mathbf{d}_{\boldsymbol{\varphi}} \\ \Delta\mathbf{d}_{\Phi} \end{bmatrix} = \begin{bmatrix} \widetilde{\mathbf{f}}_{\boldsymbol{\varphi}} \\ \mathbf{f}_{\Phi} \end{bmatrix} \tag{71}$$

for which the augmented stiffness matrix and right-hand side vector contributions are given by equation (45a). Noting that we can write the iterative update for the scalar potential field as equation (41) we can produce the Schur complement of the reduced linear system to compute the iterative displacement update as given in equation (44). Once the displacement update has been determined, it is necessary to post-process for the continuous potential field using equation (41) and for the discontinuous fields using the identities given in equation (42) followed by equation (43).

With regards to the nature of the solution scheme, we choose to solve for the displacement field before the potential. This is because computing the vector operation $\mathbf{K}_{\Phi\Phi}^{-1}\left(\bullet\right)_{\Phi}$ for the Φ sub-block of an arbitrary global vector $(\bullet)$ is cheap in comparison to $\mathbf{K}_{\boldsymbol{\varphi}\boldsymbol{\varphi}}^{-1}\left(\bullet\right)_{\boldsymbol{\varphi}}$. Although the volume of cover for Φ is larger than that

of $\boldsymbol{\varphi}$, its nature is well understood (as it derives from the Laplace-type problem $\nabla^2\Phi = 0$) and its bandwidth is much lower than that of the displacement stiffness matrix.

Equation (46) is solved using an iterative method for which only the matrix-vector operation by $\mathbf{S}$ or $\widetilde{\mathbf{S}}$ is required (as opposed to the direct expression of their inverse). To achieve this, an inner solver is required to compute the result of $\mathbf{K}_{\Phi\Phi}^{-1}(\bullet)_\Phi$ and, for the case of $\mathbf{S}$, also $\mathbf{K}_{\widetilde{p}\widetilde{J}}^{-1}(\bullet)_{\widetilde{p}}$ and $\mathbf{K}_{\widetilde{J}\widetilde{p}}^{-1}(\bullet)_{\widetilde{J}}$. The former operation is performed using the conjugate-gradient (CG) algorithm[10] in conjunction with an algebraic multi-grid (AMG) preconditioner [102], while the latter two used CG with a Jacobi preconditioner. As the problem is fully symmetric, the approximate inverse $\mathbf{S}^{-1}$ or $\widetilde{\mathbf{S}}^{-1}$ was computed using a reduced-iteration CG solver with an AMG preconditioner applied to $\mathbf{K}_{\boldsymbol{\varphi}\boldsymbol{\varphi}}$ or $\widetilde{\mathbf{K}}_{\boldsymbol{\varphi}\boldsymbol{\varphi}}$. As it is embedded within a Newton–Raphson method, the solution to the linearised problem may be inexact as the algorithm is self-correcting.

A computationally less expensive approximation of the inverse of $\mathbf{S}$ or $\widetilde{\mathbf{S}}$ is used as a preconditioner to solve equation (46). As a replacement the expensive inner inverse matrix multiplications we choose to define the approximate inverse of $\mathbf{K}_{\Phi\Phi}$ by a single sweep of its symmetric successive over-relaxation (SSOR) preconditioner, while the equivalent operation for $\mathbf{K}_{\widetilde{p}\widetilde{J}}$ and $\mathbf{K}_{\widetilde{J}\widetilde{p}}$ is performed by a sweep of their Jacobi preconditioner.

Apart from the apparent increase in the number of matrix-vector operations when solving equation (40) as opposed to equation (44), the primary difference arising from the implementation of these two schemes is the preconditioner from the $\boldsymbol{\varphi} - \boldsymbol{\varphi}$ space used for the Schur matrix. When condensation is used, we transform $\mathbf{K}_{\boldsymbol{\varphi}\boldsymbol{\varphi}} \rightarrow \widetilde{\mathbf{K}}_{\boldsymbol{\varphi}\boldsymbol{\varphi}}$ using equation (45a) which, depending on the degree of material incompressibility, may be stiff.

C. NATURE OF MESH MOTION PROBLEM

The nature of the mesh update algorithm derived from the linear elastic equations with the specialised constitutive law are established below. Substituting equation (50) into equation (48) and regrouping terms we attain

$$
\begin{aligned}
0 &= \frac{\partial}{\partial X_j}\left[\mathcal{K}_{ijkl}\frac{1}{2}\left[\frac{\partial\varphi_k}{\partial X_l}+\frac{\partial\varphi_l}{\partial X_k}\right]\right] \\
&= \frac{\partial}{\partial X_j}\left[k\left(\mathbf{X}\right)\left[\left[1-\alpha\right]\frac{1}{2}\left[\delta_{ik}\delta_{jl}+\delta_{il}\delta_{jk}\right]+\alpha\delta_{ij}\delta_{kl}\right]\frac{1}{2}\left[\frac{\partial\varphi_k}{\partial X_l}+\frac{\partial\varphi_l}{\partial X_k}\right]\right] \\
&= k\left(\mathbf{X}\right)\left[\left[1-\alpha\right]\frac{\partial}{\partial X_j}\frac{1}{2}\left[\frac{\partial\varphi_i}{\partial X_j}+\frac{\partial\varphi_j}{\partial X_i}\right]+\alpha\frac{\partial^2\varphi_j}{\partial X_i\partial X_j}\right] \\
&\equiv k\left(\mathbf{X}\right)\left[\frac{1}{2}\left[1-\alpha\right]\frac{\partial^2\varphi_i}{\partial X_j\partial X_j}+\frac{1}{2}\left[1+\alpha\right]\frac{\partial^2\varphi_j}{\partial X_i\partial X_j}\right] \quad .
\end{aligned}
$$

From the last line it is deduced that the natural limiting values for the blend coefficient are $\alpha \in [-1, 1]$.

REFERENCES

1. Lochmatter P. Development of a shell-like electroactive polymer (eap) actuator. PhD Thesis, Swiss Federal Institute of Technology, Zurich 2007, .
2. Böse H, Rabindranath R, Ehrlich J. Soft magnetorheological elastomers as new actuators for valves. *Journal of Intelligent Material Systems and Structures* 2012; **23**(9):989–994, .

[10] With reference to equation (38) and the surrounding discussion, depending on the chosen material laws and constitutive parameters $\mathbf{K}_{\Phi\Phi}$ may not necessarily be either positive or negative definite. Therefore, the choice of solver used for this operation should either be made on a case-by-case basis or simply a more robust solver, such as GMRES, could be utilised.

3. Carlson JD, Jolly MR. MR fluid, foam and elastomer devices. *Mechatronics* 2000; **10**(4):555–569, .
4. Bar-Cohen Y. Electroactive polymers as artificial muscles: A review. *Journal of Spacecraft and Rockets* 2002; **39**(6):822–827, .
5. Nguyen VQ, Ahmed AS, Ramanujan RV. Morphing soft magnetic composites. *Advanced Materials* 2012; **24**(30):4041–4054, .
6. Müller R, Xu B, Gross D, Lyschik M, Schrade D, Klinkel S. Deformable dielectrics - optimization of heterogeneities. *International Journal of Engineering Science* 2010; **48**(7-8):647–657, .
7. Wang H, Lei M, Cai S. Viscoelastic deformation of a dielectric elastomer membrane subject to electromechanical loads. *Journal of Applied Physics* 2013; **113**(21):213 508, .
8. Jolly MR, Carlson JD, Munoz BC. A model of the behaviour of magnetorheological materials. *Smart Materials and Structures* 1996; **5**(5):607–614.
9. Ginder JM, Clark SM, Schlotter WF, Nichols ME. Magnetostrictive phenomena in magnetorheological elastomers. *International Journal of Modern Physics B* 2002; **16**(17–18):2412–2418, .
10. Varga Z, Filipcsei G, Zrínyi M. Magnetic field sensitive functional elastomers with tuneable elastic modulus. *Polymer* 2006; **47**:227–233, .
11. Danas K, Kankanala SV, Triantafyllidis N. Experiments and modeling of iron-particle-filled magnetorheological elastomers. *Journal of the Mechanics and Physics of Solids* 2012; **60**(1):120–138, .
12. Boczkowska A, Awietjan S. *Advanced Elastomers - Technology, Properties and Applications*, chap. 6: Microstructure and Properties of Magnetorheological Elastomers. InTech, 2012; 147–180.
13. Wissler MT. Modeling dielectric elastomer actuators. PhD Thesis, Swiss Federal Institute of Technology, Zurich 2007. URL `http://www.empa.ch/plugin/template/empa/*/78910`.
14. Dorfmann A, Ogden RW. Nonlinear magnetoelastic deformations of elastomers. *Acta Mechanica* 2003; **167**(1-2):13–28, .
15. Bustamante R, Dorfmann A, Ogden RW. A nonlinear magnetoelastic tube under extension and inflation in an axial magnetic field: numerical solution. *Journal of Engineering Mathematics* 2007; **59**(1):139–153, .
16. Kankanala SV, Triantafyllidis N. On finitely strained magnetorheological elastomers. *Journal of the Mechanics and Physics of Solids* 2004; **52**(12):2869 – 2908, .
17. Galipeau E. Non-linear homogenization of magnetorheological elastomers at finite strain. PhD Thesis, University of Pennsylvania 2012. URL `http://repository.upenn.edu/edissertations/634`, publicly Accessible Penn Dissertations. Paper 634.
18. Saxena P, Pelteret JPV, Steinmann P. Modelling of iron-filled magneto-active polymers with a dispersed chain-like microstructure. *European Journal of Mechanics A/Solids* March–April 2015; **50**:132–151, .
19. Yang E, Frecker M, Mockensturm E. Finite element and experimental analyses of non-axisymmetric dielectric elastomer actuators. *Smart Structures and Materials*, International Society for Optics and Photonics, 2006; 61 680H–61 680H, .
20. Vu DK, Steinmann P, Possart G. Numerical modelling of non-linear electroelasticity. *International Journal for Numerical Methods in Engineering* 2007; **70**(6):685–704, .
21. Zwecker S, Müller R, Klinkel S. Nonlinear finite element simulation of thin dielectric elastomer structures. *Proceedings of 1st Young Researcher Symposium by Center for Mathematical and Computational Modelling*, Balle N F Marheineke, Kienle F, Schmidt K, Tschauder N (eds.), Kaiserslautern, Germany, 2011. URL `http://ceur-ws.org/Vol-750/YRS2011_proceedings.pdf`.
22. Ask A, Menzel A, Ristinmaa M. Electrostriction in electro-viscoelastic polymers. *Mechanics of Materials* 2012; **50**:9–21, .
23. Hossain M, Vu DK, Steinmann P. Experimental study and numerical modelling of VHB 4910 polymer. *Computational Materials Science* 2012; **59**:65–74, .
24. Skatulla S, Sansour C, Arockiarajan A. A multiplicative approach for nonlinear electro-elasticity. *Computer Methods in Applied Mechanics and Engineering* 2012; **245**:243–255.
25. Büschel A, Klinkel S, Wagner W. Dielectric elastomers–numerical modeling of nonlinear visco-electroelasticity. *International Journal for Numerical Methods in Engineering* 2013; **93**(8):834–856, .
26. Bustamante R, Dorfmann A, Ogden RW. Numerical solution of finite geometry boundary-value problems in nonlinear magnetoelasticity. *International Journal of Solids and Structures* 2011; **48**(6):874–883, .
27. Barham MI, White DA, Steigmann DJ. Finite element modeling of the deformation of magnetoelastic film. *Journal of Computational Physics* 2010; **229**(18):6193 – 6207, .
28. Ortigosa R, Gil AJ. A new framework for large strain electromechanics based on convex multi-variable strain energies: Finite element discretisation and computational implementation. *Computer Methods in Applied Mechanics and Engineering* 2015; .

29. Rodríguez-Ramos R, Pobedria BE, Padilla P, Bravo-Castillero J, Guinovart-Díaz R, Maugin GA. Variational principles for nonlinear piezoelectric materials. *Archive of Applied Mechanics* 2004; **74**(3-4):191–200, .
30. Yang JS, Batra RC. Mixed variational principles in non-linear electroelasticity. *International Journal of Non-linear Mechanics* 1995; **30**(5):719–725, .
31. Poya R, Gil AJ, Ledger PD. A computational framework for the analysis of linear piezoelectric beams using hp-FEM. *Computers & Structures* 2015; **152**:155–172, .
32. Vogel F, Göktepe S, Steinmann P, Kuhl E. Modeling and simulation of viscous electro-active polymers. *European Journal of Mechanics A/Solids* 2014; .
33. Vu DK. A study on nonlinear electro-elastostatics: Theory and numerical simulation. Habilitation, Friedrich Alexander University of Erlangen-Nrnberg 2014.
34. Kofod G, Sommer-Larsen P. Silicone dielectric elastomer actuators: Finite-elasticity model of actuation. *Sensors and Actuators A: Physical* 2005; **122**(2):273–283, .
35. Pao YH. Electromagnetic forces in deformable continua. *Mechanics today*, Nemat-Nasser S (ed.). Pergamon Press: New York, 1978.
36. Maugin GA. A continuum theory of deformable ferrimagnetic bodies. I. Field equations. *Journal of Mathematical Physics* 1975; **17**(9):1727–1738, .
37. Salas E, Bustamante R. Numerical solution of some boundary value problems in nonlinear magneto-elasticity. *Journal of Intelligent Material Systems and Structures* 2014; .
38. Vu DK, Steinmann P. A 2-d coupled BEM–FEM simulation of electro-elastostatics at large strains. *Comput. Meth. Appl. Mech. Eng* 2010; **199**(17-20):1124–1133, .
39. Vu DK, Steinmann P. On 3-d coupled BEM–FEM simulation of nonlinear electro-elastostatics. *Computer Methods in Applied Mechanics and Engineering* 2012; **201**:82–90, .
40. Steinmann P. Computational nonlinear electro-elasticity – getting started: Mechanics and Electrodynamics of Magneto- and Electro-elastic Materials. *Mechanics and Electrodynamics of Magneto- and Electro-elastic Materials*, *CISM Courses and Lectures*, vol. 527, Ogden RW, Steigmann DJ (eds.). 1st edn., Springer-Verlag Wien: Vienna, 2011, . ISBN: 978-3-7091-0700-3.
41. Kovetz A. *Electromagnetic theory*. Oxford University Press: Oxford and New York, 2000. ISBN: 0-19-850603-1.
42. Vu DK, Steinmann P. On the spatial and material motion problems in nonlinear electro-elastostatics with consideration of free space. *Mathematics and Mechanics of Solids* 2012; **17**(8):803–823, .
43. Bossavit A. *Computational Electromagnetism. Variational Formulations, Complementarity, Edge Elements*, *Electromagnetism Series*, vol. 2. 1st edn., Academic Press: San Diego, 1998. ISBN-13: 978-0121187101.
44. Ogden RW. Advanced Course on Mechanics and Electrodynamics of Magneto- and Electro-elastic Materials. *Mechanics and Electrodynamics of Magneto- and Electro-elastic Materials*, *CISM Courses and Lectures*, vol. 527, Ogden RW, Steigmann DJ (eds.). 1st edn., Springer-Verlag Wien: Vienna, 2011, . ISBN: 978-3-7091-0700-3.
45. Bustamante R, Dorfmann A, Ogden R. Nonlinear electroelastostatics: a variational framework. *Zeitschrift für angewandte Mathematik und Physik* 2009; **60**(1):154–177, .
46. Vogel F, Bustamante R, Steinmann P. On some mixed variational principles in magneto-elastostatics. *International Journal of Non-Linear Mechanics* 2013; **51**(0):157 – 169, .
47. Dorfmann A, Ogden RW. Nonlinear electroelasticity. *Acta Mechanica* 2005; **174**(3-4):167–183, .
48. Vu DK, Steinmann P. Nonlinear electro- and magneto-elastostatics: Material and spatial settings. *International Journal of Solids and Structures* 2007; **44**(24):7891–7905, .
49. Dorfmann A, Ogden RW. Nonlinear magnetoelastic deformations. *The Quarterly Journal of Mechanics and Applied Mathematics* 2004; **57**(4):599–622, .
50. Brown WF. *Magnetoelastic interactions*. Springer: Berlin and Heidelberg and New York, 1966, . ISBN: 978-3-642-87398-0.
51. Maugin G. On the equations of the electrodynamics of deformable bodies of finite extent. *Journal de Mécanique* 1977; **16**.
52. Eringen AC, Maugin GA. *Electrodynamics of Continua I: Foundations and Solid Media*. Springer: Berlin, 1990, . ISBN: 978-1-4612-7923-5.
53. Steigmann DJ. Equilibrium theory for magnetic elastomers and magnetoelastic membranes. *International Journal of Non-Linear Mechanics* 2004; **39**(7):1193–1216, .
54. Wriggers P. *Nonlinear finite element methods*, vol. 4. Springer, 2008, .
55. Holzapfel GA. *Nonlinear solid mechanics*. John Wiley & Sons Ltd.: West Sussex, England, 2007. ISBN: 0-471-82304-X.
56. Vogel F, Pelteret JPV, Kaessmair S, Steinmann P. Magnetic force and torque on particles subject to a magnetic field. *European Journal of Mechanics A/Solids* November–December 2014; **48**:23–37, .
57. Maugin GA. *Continuum mechanics of electromagnetic solids*. North-Holland, 1988. ISBN: 0444703993.

58. Dorfmann A, Ogden RW. Nonlinear electroelastic deformations. *Journal of Elasticity* 2006; **82**(2):99–127, .
59. Simo JC, Taylor RL, Pister KS. Variational and projection methods for the volume constraint in finite deformation elasto-plasticity. *Computer Methods in Applied Mechanics and Engineering* 1985; **51**:177–208, .
60. Miehe C. Aspects of the formulation and finite element implementation of large strain isotropic elasticity. *International Journal for Numerical Methods in Engineering* 1994; **37**(12):1981–2004, .
61. Schröder J, Neff P. Invariant formulation of hyperelastic transverse isotropy based on polyconvex free energy functions. *International journal of solids and structures* 2003; **40**(2):401–445, .
62. Bonet J, Gil AJ, Ortigosa R. A computational framework for polyconvex large strain elasticity. *Computer Methods in Applied Mechanics and Engineering* 2015; **283**:1061–1094.
63. Itskov M, Aksel N. A class of orthotropic and transversely isotropic hyperelastic constitutive models based on a polyconvex strain energy function. *International journal of solids and structures* 2004; **41**(14):3833–3848.
64. Gil AJ, Ortigosa R. A new framework for large strain electromechanics based on convex multi-variable strain energies: Variational formulation and material characterisation. *Computer Methods in Applied Mechanics and Engineering* 2016; .
65. Itskov M, Khiêm VN. A polyconvex anisotropic free energy function for electro-and magneto-rheological elastomers. *Mathematics and Mechanics of Solids* 2014; **27**:1–12, .
66. Otténio M, Destrade M, Ogden R. Incremental magnetoelastic deformations, with application to surface instability. *Journal of Elasticity* 2008; **90**(1):19–42, .
67. Rudykh S, Bertoldi K. Stability of anisotropic magnetorheological elastomers in finite deformations: A micromechanical approach. *Journal of the Mechanics and Physics of Solids* 2013; **61**(4):949–967, .
68. Miehe C, Vallicotti D, Zäh D. Computational structural and material stability analysis in finite electro-elasto-statics of electro-active materials. *International Journal for Numerical Methods in Engineering* 2015; **102**(10):1605–1637, .
69. Sansour C. On the physical assumptions underlying the volumetric-isochoric split and the case of anisotropy. *European Journal of Mechanics – A/Solids* 2008; **27**:28–39, .
70. de Veubeke BMF. Diffusion des inconnues hyperstatiques dans les voilures á longerons couplés. *Technical Report*, Bull. Serv. Technique de l'Aéronautique 1951. Pp. 56.
71. Nagtegaal JC, Parks DM, Rice JR. On numerically accurate finite element solutions in the fully plastic range. *Computer methods in applied mechanics and engineering* 1974; **4**(2):153–177.
72. Simo JC, Taylor RL. Quasi-incompressible finite elasticity in principal stretches. Continuum basis and numerical algorithms. *Computer Methods in Applied Mechanics and Engineering* 1991; **85**:273–310, .
73. Brink U, Stein E. On some mixed finite element methods for incompressible and nearly incompressible finite elasticity. *Computational Mechanics* 1996; **19**(1):105–119, .
74. Schwarz A, Schröder J, Starke G. A modified least-squares mixed finite element with improved momentum balance. *International journal for numerical methods in engineering* 2010; **81**(3):286–306, .
75. Schröder J, Wriggers P, Balzani D. A new mixed finite element based on different approximations of the minors of deformation tensors. *Computer Methods in Applied Mechanics and Engineering* 2011; **200**(49):3583–3600, .
76. Ask A, Menzel A, Ristinmaa M. Phenomenological modeling of viscous electrostrictive polymers. *International Journal of Non-Linear Mechanics* 2012; **47**(2):156–165, .
77. Ask A, Denzer R, Menzel A, Ristinmaa M. Inverse-motion-based form finding for quasi-incompressible finite electroelasticity. *International Journal for Numerical Methods in Engineering* 2013; **94**(6):554–572, .
78. Jabareen M. Finite element modeling of the electromechanical coupling in electroactive polymers. *2nd ECCOMAS Young Investigators Conference (YIC 2013)*, ECCOMAS: Bordeaux, France, 2013; 1–4.
79. Benzi M, Golub GH, Liesen J. Numerical solution of saddle point problems. *Acta numerica* 2005; **14**:1–137.
80. Bustamante R, Ogden R. Nonlinear magnetoelastostatics: Energy functionals and their second variations. *Mathematics and Mechanics of Solids* 2012; **18**(7):760–772, .
81. Hughes TJ. *The Finite Element Method: Linear Static and Dynamic Finite Element Analysis*. Dover Publications Inc.: New York, USA, 2000. ISBN: 978-0486411811.
82. Simo J. On a fully three-dimensional finite-strain viscoelastic damage model: formulation and computational aspects. *Computer methods in applied mechanics and engineering* 1987; **60**(2):153–173, .
83. Saad Y. *Iterative Methods for Sparse Linear Systems*. 2nd edn., The Society for Industrial and Applied Mathematics, 2003.
84. Bangerth W, Hartmann R, Kanschat G. deal.II – a general purpose object oriented finite element library. *ACM Trans. Math. Softw.* 2007; **33**(4):24/1–24/27, .
85. Bangerth W, Heister T, Heltai L, Kanschat G, Kronbichler M, Maier M, Turcksin B, Young T. The deal.ii library, version 8.2. *Archive of Numerical Software* 2015; **3**(100), .

86. Heroux MA, Bartlett RA, Howle VE, Hoekstra RJ, Hu JJ, Kolda TG, Lehoucq RB, Long KR, Pawlowski RP, Phipps ET, *et al.*. An overview of the Trilinos project. *ACM Transactions on Mathematical Software* 2005; **31**:397–423, .
87. Heroux MA. AztecOO user's guide. *Technical Report SAND2004-3796*, Sandia National Laboratories 2007. URL `https://trilinos.org/oldsite/packages/aztecoo/AztecOOUserGuide.pdf`.
88. Bangerth W, Kayser-Herold O. Data structures and requirements for *hp* finite element software. *ACM Trans. Math. Softw.* 2009; **36**(1):4/1–4/31, .
89. Jasak H, Tuković u. Automatic mesh motion for the unstructured finite volume method. *Transactions of Famena* 2006; **30**(2):1–20.
90. Löhner R, Yang C. Improved ALE mesh velocities for moving bodies. *Communications in Numerical Methods in Engineering* 1996; **12**(10):599–608, .
91. Johnson AA, Tezduyar TE. Mesh update strategies in parallel finite element computations of flow problems with moving boundaries and interfaces. *Computer Methods in Applied Mechanics and Engineering* 1994; **119**(1-2):73–94, .
92. Bazilevs Y, Calo V, Hughes T, Zhang Y. Isogeometric fluid-structure interaction: Theory, algorithms, and computations. *Computational Mechanics* 2008; **43**(1):3–37, .
93. Knupp P, Freitag-Diachin L, Tidwell B. Mesquite mesh quality improvement toolkit user's guide. *Technical Report*, Sandia National Laboratories 2013. URL `https://software.sandia.gov/mesquite/doc-2.99/users-guide.pdf`.
94. Bustamante R. Mathematical modelling of boundary conditions for magneto-sensitive elastomers: variational formulations. *Journal of Engineering Mathematics* 2009; **64**(3):285–301, .
95. Bustamante R. A variational formulation for a boundary value problem considering an electro-sensitive elastomer interacting with two bodies. *Mechanics Research Communications* 2009; **36**(7):791–795, .
96. Stimpson CJ, Ernst CD, Knupp P, Pébay PP, Thompson D. The verdict geometric quality library. *Technical Report SAND2007-1751*, Sandia National Laboratories 2007. URL `http://www.csimsoft.com/download?file=Documents/sand20071751.pdf`.
97. Hossain M, Vu DK, Steinmann P. A comprehensive characterization of the electro- mechanically coupled properties of VHB 4910 polymer. *Archive of Applied Mechanics* 2014; .
98. Volokh KY. On electromechanical coupling in elastomers. *Journal of Applied Mechanics* 2012; **79**(4):044 507, .
99. Arruda EM, Boyce MC. A three-dimensional constitutive model for the large stretch behavior of rubber elastic materials. *Journal of the Mechanics and Physics of Solids* 1993; **41**(2):389–412, .
100. Mitsumata T, Ohori S, Honda A, Kawai M. Magnetism and viscoelasticity of magnetic elastomers with wide range modulation of dynamic modulus. *Soft Matter* 2013; **9**(3):904–912, .
101. Meeker D. *Finite Element Method Magnetics. Version 4.2. User's Manual* February 2009. URL `http://www.femm.info/Archives/doc/manual42.pdf`.
102. Gee MW, Siefert CM, Hu JJ, Tuminaro RS, Sala MG. ML 5.0 smoothed aggregation user's guide. *Technical Report SAND2006-2649*, Sandia National Laboratories 2006. URL `https://trilinos.org/oldsite/packages/ml/mlguide5.pdf`.

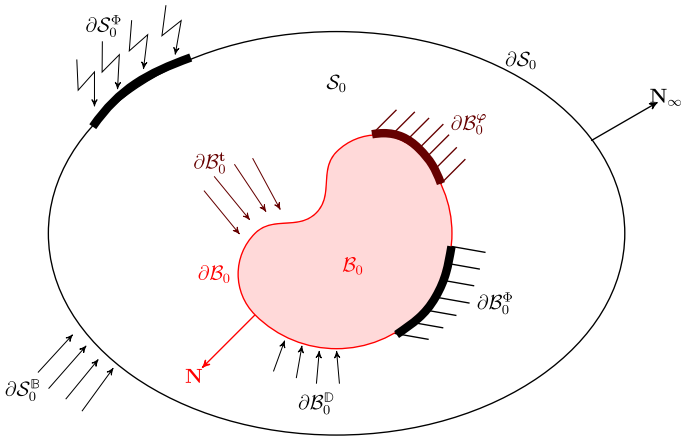

Figure 1. Domain definition, with illustration of the deformable body $\mathcal{B}_0$ immersed in a electromagnetically permeable medium $\mathcal{S}_0$.

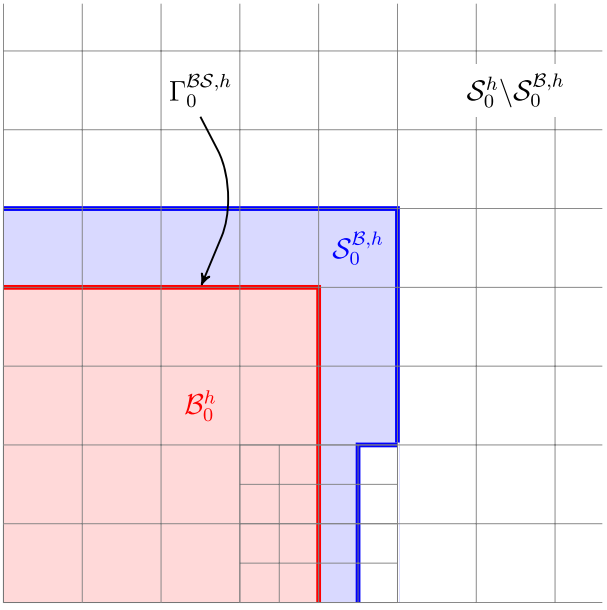

Figure 2. Specialised discretisation of the problem domain using finite elements. The free space has been partitioned, with the finite-element treatment of the layer of cells directly adjacent to the solid body being different to that of the rest of the subdomain. Note that the definition of $\mathcal{S}_0^{\mathcal{B},h}$ must follow any h-refinement that occurs across the solid-free space interface.

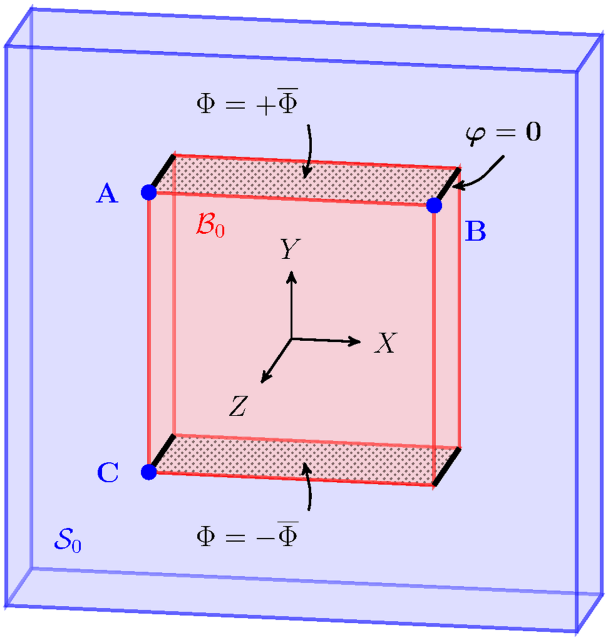

Figure 3. Representative geometry of pinned square plate in free space

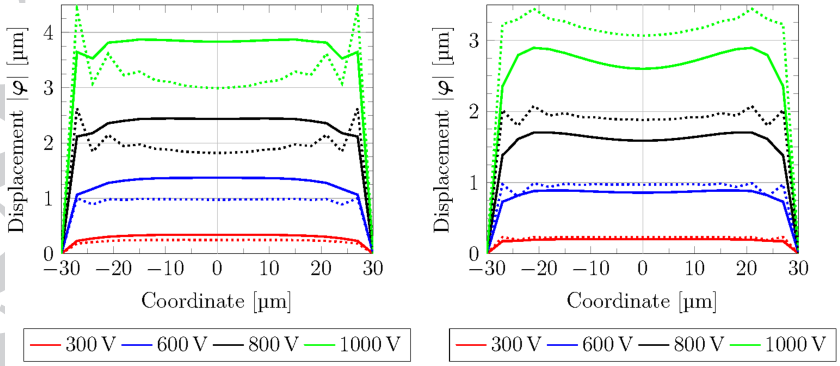

(a) Edge **A** − **B** (b) Edge **A** − **C**

Figure 4. Total displacement magnitude along plate edges. Solid lines indicate compressible case ($\lambda = 60\,\mathrm{kPa}$) and dotted lines indicate result for quasi-incompressible case ($\lambda = 249.95\,\mathrm{MPa}$).

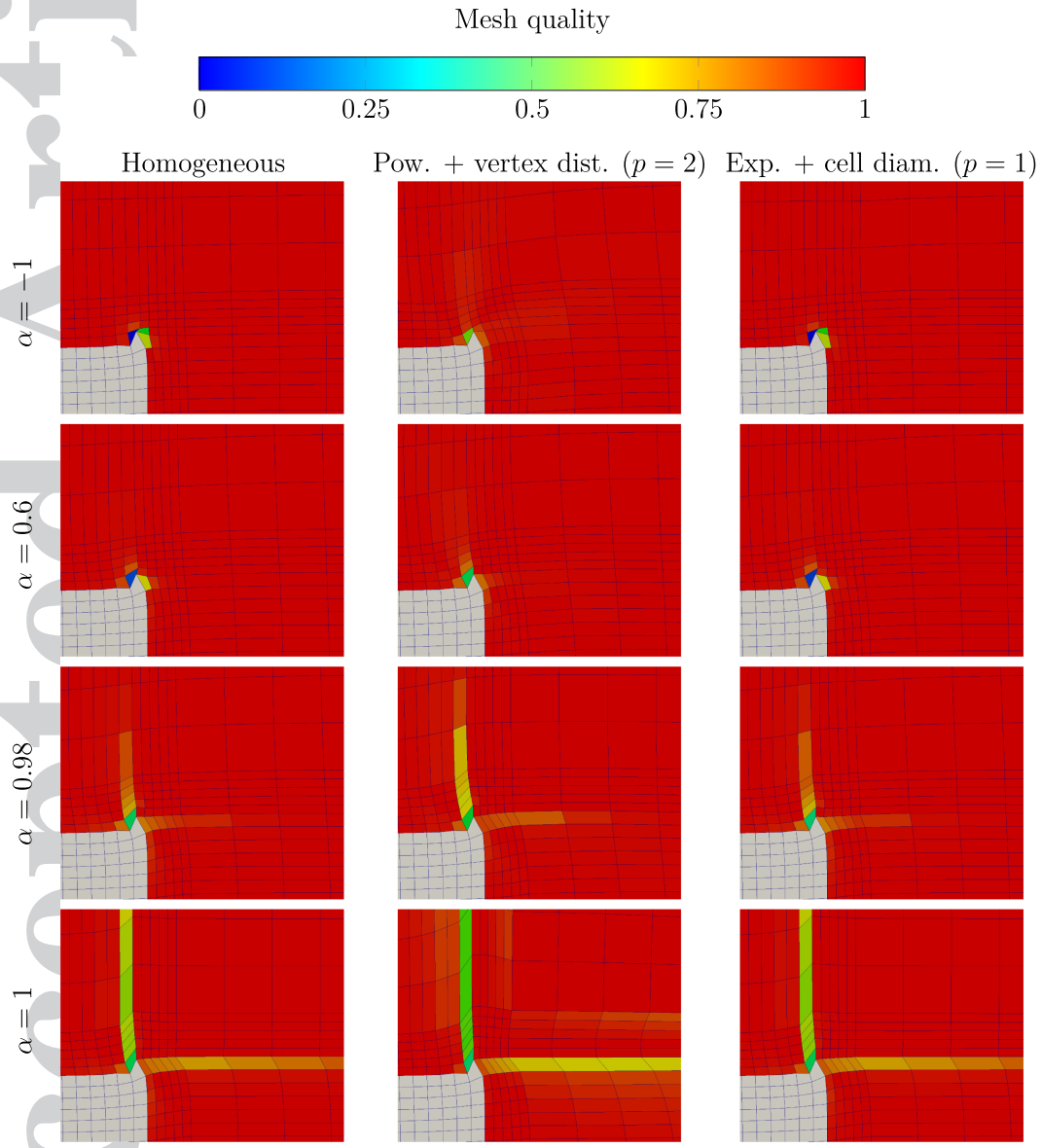

Figure 5. Comparison of a selection of mesh update methods for $\Delta\Phi = 1000\,\mathrm{V}$ (compressible case; $\lambda = 60\,\mathrm{kPa}$). The boundary layer mesh surrounding the elastic body is clearly visible.

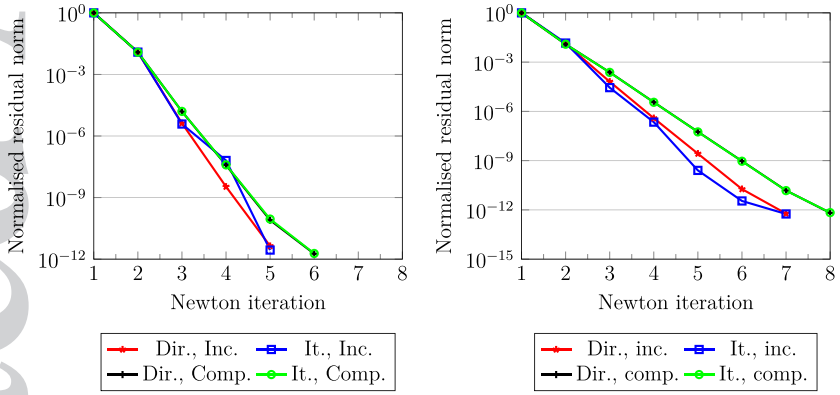

(a) Load step 6 ($\Delta\Phi = 360\,\mathrm{V}$) (b) Load step 10 ($\Delta\Phi = 600\,\mathrm{V}$)

Figure 6. Convergence of the normalised residual norm $\frac{|\mathbf{r}|}{|\mathbf{r}_1|}$ at different load steps. Cases for which the direct and iterative solver were used are denoted "Dir." and "It." respectively, while the incompressible and compressible cases are respectively delineated by "inc." and "comp.". The maximum potential difference is $\max \Delta\Phi = 600\,\mathrm{V}$.

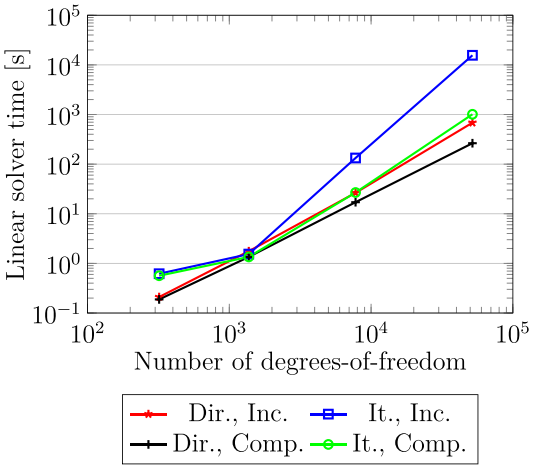

Figure 7. Influence of uniform h-refinement on linear solver time. The maximum potential difference is $\max \Delta\Phi = 600\,\mathrm{V}$.

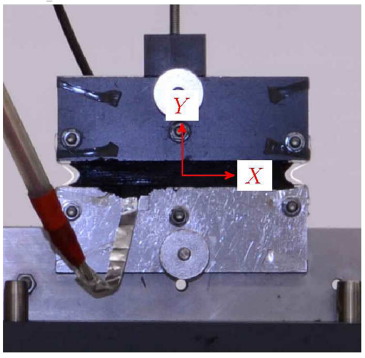

(a) Laterally prestretched (mechanically loaded) EAP sample within the experimental apparatus.

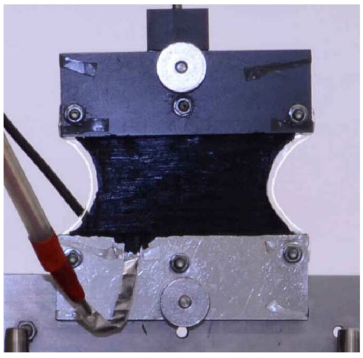

(b) Laterally and vertically prestretched EAP sample within the experimental apparatus.

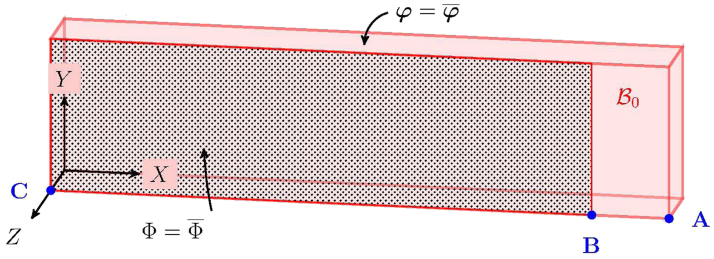

(c) Representation of $\frac{1}{8}$ of the EAP geometry as domain for boundary value problem.

Figure 8. Electro-active polymer strip with conductive surface coating. An unpainted (non-conductive) strip can be observed at the edge of the material.

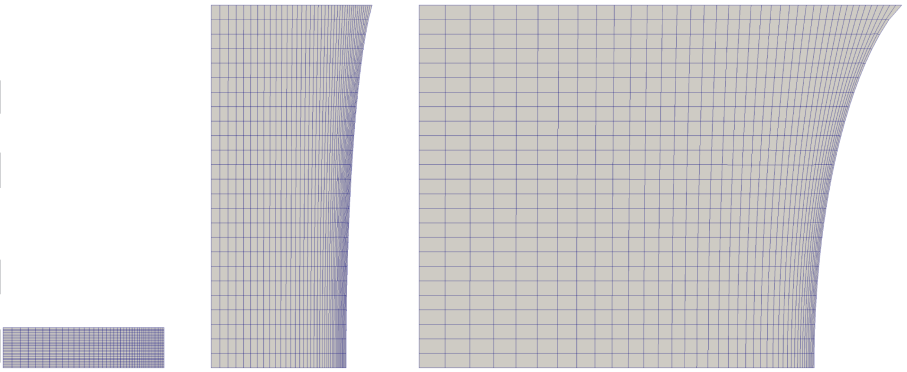

(a) $t = 0\,\mathrm{s}$ (b) $t = 30\,\mathrm{s}$ (c) $t = 60\,\mathrm{s}$

Figure 9. Deformation of the strip during stretching phase

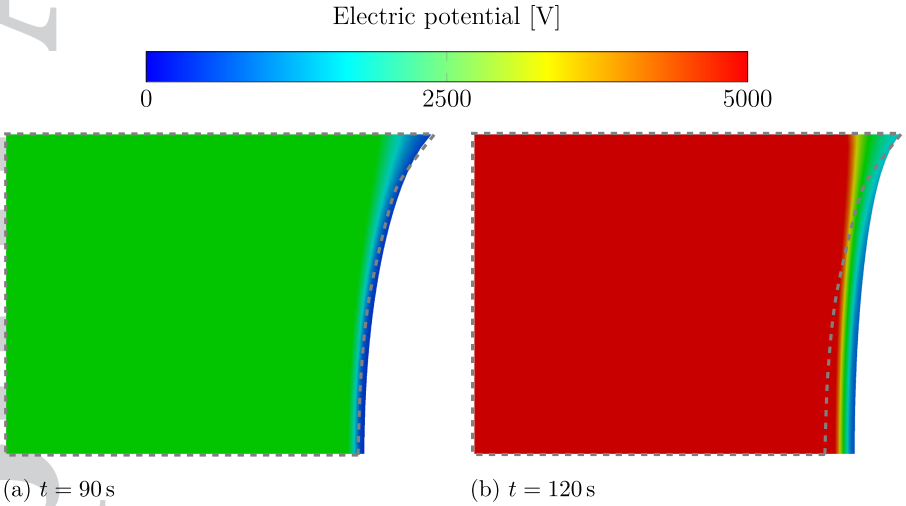

(a) $t = 90\,\mathrm{s}$ (b) $t = 120\,\mathrm{s}$

Figure 10. Deformation of the strip during application of electric potential. The position of the polymer after prestretch ($t = 60\,\mathrm{s}$) indicated by the dashed outline.

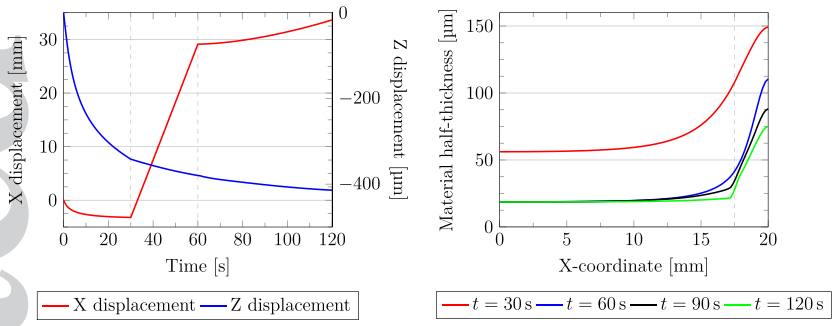

(a) Displacement at point **A**

(b) Material half-thickness along line **C**−**B**−**A**

Figure 11. Deformation recorded in various regions of the geometry

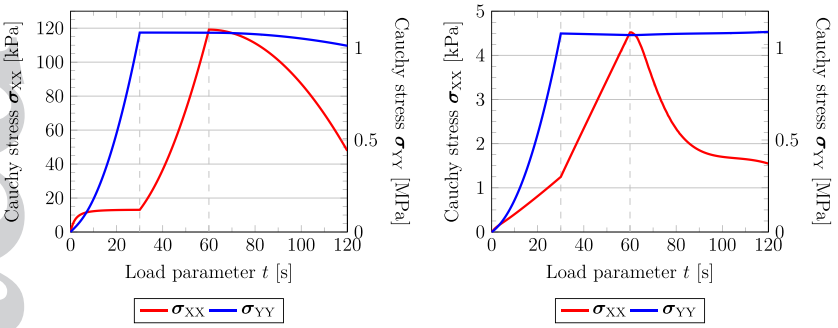

(a) Origin **O** (b) Boundary point **A**

Figure 12. Stress history at various points in the geometry

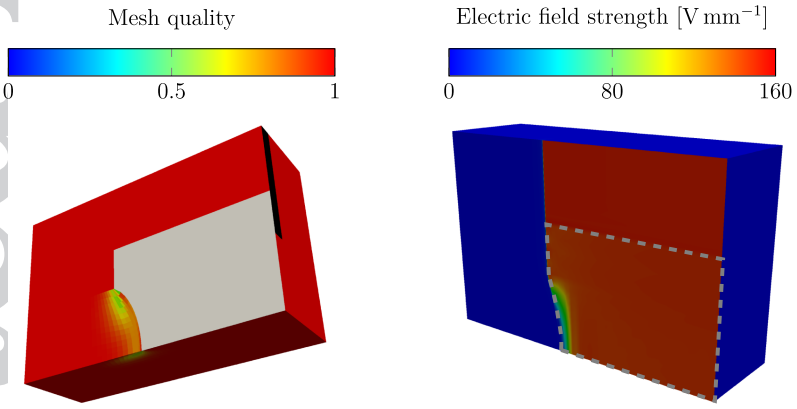

(a) Deformed geometry and free space mesh quality at $t = 60\,\mathrm{s}$

(b) Electric field at $t = 120\,\mathrm{s}$. The edge of the material is indicated by the dashed line.

Figure 13. Deformation of the EAP strip with the free space and mechanical clamps considered.

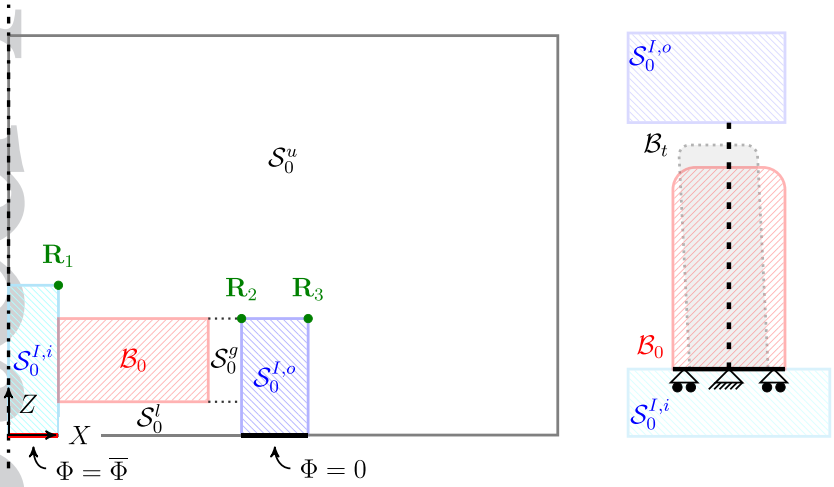

Figure 14. A scale representation of the cross-section of magneto-active polymer valve geometry and boundary conditions. The original position of the polymer $\mathcal{B}_0$ is shown in red and its expected displaced configuration $\mathcal{B}_t$ shown in grey.

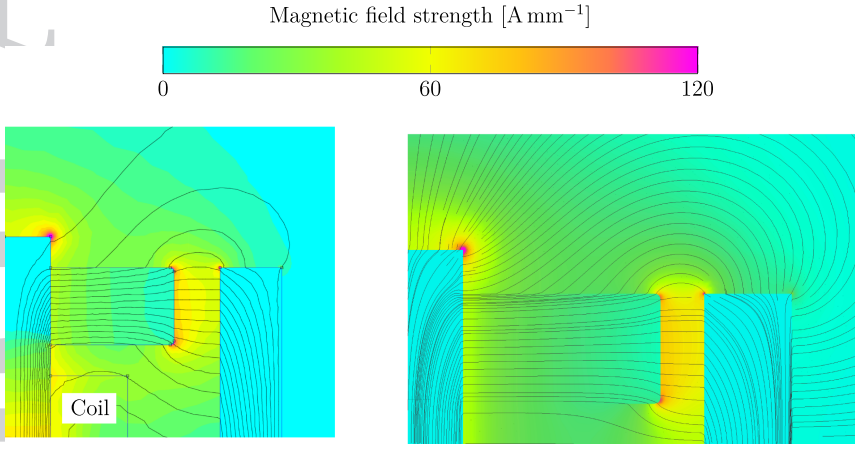

(a) Vector potential formulation driven by a 5 A current through a copper coil with 0.5 mm wire thickness and 500 turns.

(b) Magnetic scalar potential formulation with $\overline{\Phi} = 310$ A.

Figure 15. Simulation of valve under equivalent static conditions (zero-deformation) using the vector potential (curl) formulation (FEMM [101]) and the magnetic scalar potential formulation. Magnetic flux lines are shown in black.

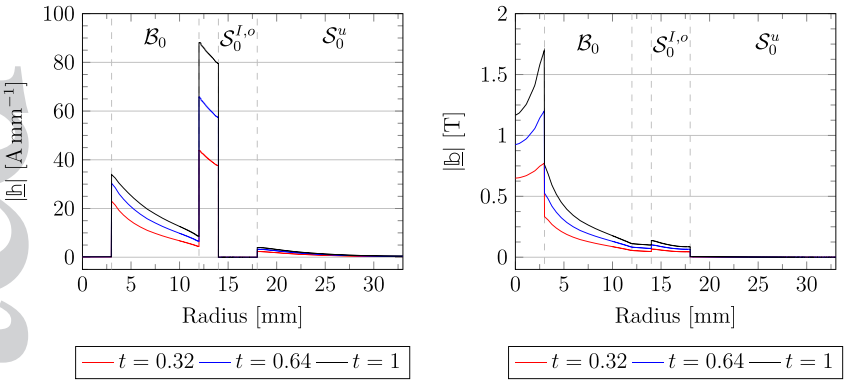

(a) Spatial magnetic field strength (b) Spatial magnetic induction

Figure 16. Magnetic quantities measured radially (along reference coordinates) at the height $Z = 4.5\,\mathrm{mm}$.

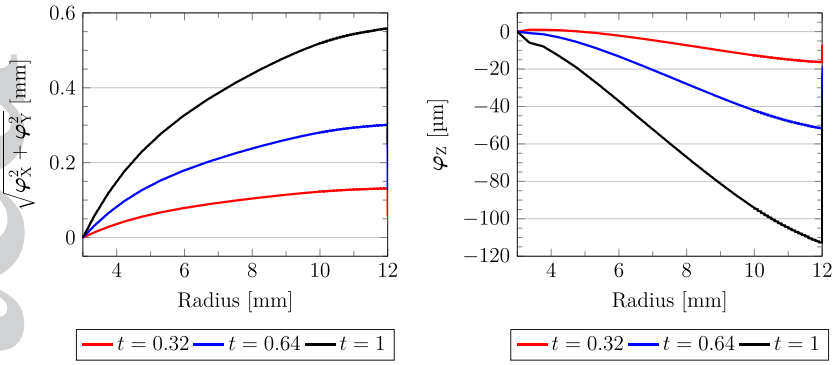

(a) Radial displacement (b) Axial displacement

Figure 17. Deformation measured radially (along reference coordinates) at axial distance $Z = 4.5\,\mathrm{mm}$.

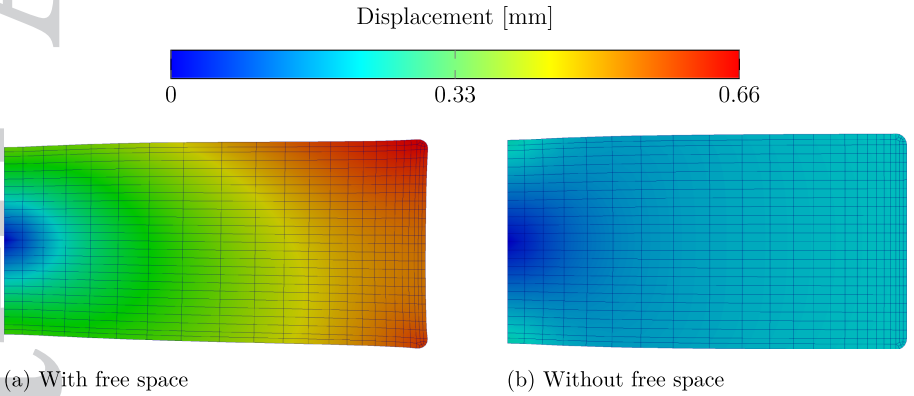

(a) With free space (b) Without free space

Figure 18. Polymer displacement solution with and without representation of the surrounding free space and iron components. For the case without free space, the potential prescribed on the polymer inner and outer surfaces was $\Phi^I = 116$ A and $\Phi^O = 309$ A respectively. With reference to figure 14, this equates to Φ^I being applied on $\overline{\mathcal{B}_0} \cap \overline{\mathcal{S}_0^{I,i}}$ and Φ^O being prescribed on $\overline{\mathcal{B}_0} \cap \overline{\mathcal{S}_0^g}$. The chosen values were obtained from the final solution for the problem that included free space.

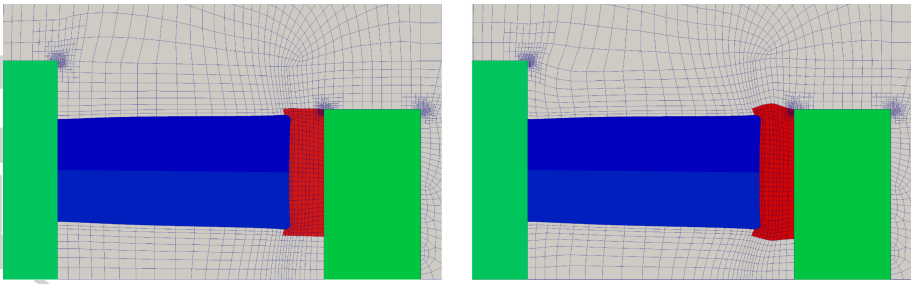

(a) $\alpha = -1, p = 1.25$ (b) $\alpha = 0.98, p = 2$

Figure 19. Comparison of free space mesh update using two choices of blending parameter. The gap between the polymer and outer yoke is highlighted in red. In both cases the stiffness function was given by the distance to the nearest solid or "pseudo-solid" vertex and defined by the power law listed in equation $(51)_2$.

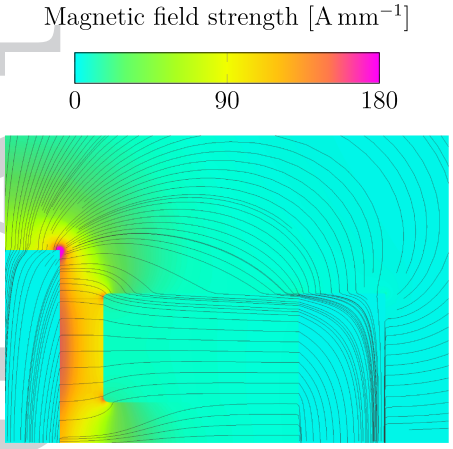

(a) Magnetic field and flux lines for magneto-static case with $\overline{\Phi} = 310\,\mathrm{A}$.

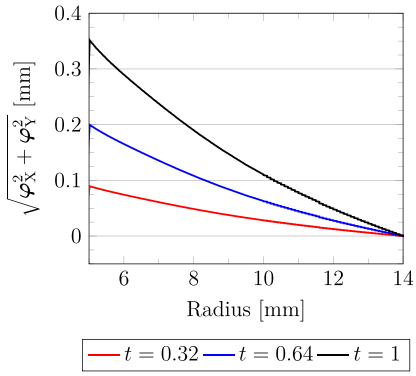

(b) Radial displacement

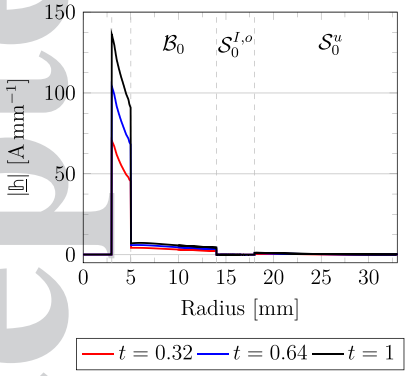

(c) Spatial magnetic field strength

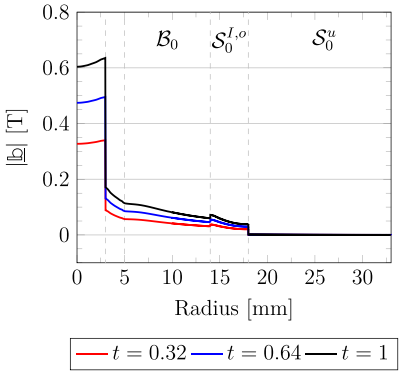

(d) Spatial magnetic induction

Figure 20. Evaluation of alternative design for valve. Measurements were taken radially (along reference coordinates) at the height $Z = 4.5\,\mathrm{mm}$.

Table I. Finite element basis applied to subdomains. The element types FE_Q and FE_DGM are respectively the continuous Lagrange FE and discontinuous monomial FE. The polynomial order is denoted by n and vector elements are highlighted by bold font.

Field	$\boldsymbol{\varphi}$		$\widetilde{p}$		$\widetilde{J}$		Φ
Subdomain			Coupled problem				
$\overline{\mathcal{B}_0^h}$	**FE_Q** (n)	$\times$	FE_DGM $(n-1)$	$\times$	FE_DGM $(n-1)$	$\times$	FE_Q (n)
$\overline{\mathcal{S}_0^{\mathcal{B},h}}$	**FE_Q** (n)	$\times$	—	$\times$	—	$\times$	FE_Q (n)
$\overline{\mathcal{S}_0^h}\backslash\overline{\mathcal{S}_0^{\mathcal{B},h}}$	**—**	$\times$	—	$\times$	—	$\times$	FE_Q (n)
			Mesh motion problem				
$\overline{\mathcal{B}_0^h}$	**—**	$\times$	—	$\times$	—	$\times$	—
$\overline{\mathcal{S}_0^{\mathcal{B},h}}$	**FE_Q** (n)	$\times$	—	$\times$	—	$\times$	—
$\overline{\mathcal{S}_0^h}\backslash\overline{\mathcal{S}_0^{\mathcal{B},h}}$	**FE_Q** (n)	$\times$	—	$\times$	—	$\times$	—

Table II. Comparison of a selection of mesh update methods (compressible case; $\lambda = 60\,\mathrm{kPa}$). The worst quality cell was computed using the scaled Jacobian metric.

	Homogeneous	Power				Exponential			
d	–	Vertex distance		Cell diameter		Vertex distance		Cell diameter	
$\alpha \backslash p$	–	1	2	1	2	1	2	1	2
-1	-0.496	0.040	0.620	-0.270	0.119	-0.500	-0.490	-0.440	-0.252
0	-0.204	0.156	0.437	-0.061	0.086	-0.208	-0.211	-0.170	-0.117
0.6	0.083	0.249	0.409	0.128	0.213	0.071	0.060	0.067	0.089
0.9	0.294	0.340	0.431	0.297	0.351	0.278	0.265	0.257	0.266
0.98	0.387	0.390	0.446	0.386	0.422	0.376	0.367	0.360	0.364
1	0.408	0.372	0.369	0.371	0.365	0.405	0.403	0.399	0.388

Table III. Number of Newton iterations needed at each fixed load step using different approaches to compute the tangent. The maximum potential difference is $\max \Delta\Phi = 600\,\mathrm{V}$. Load steps for which divergence was observed are denoted by "div.".

	Incompressible		Compressible	
Load step	Approximate tangent	Exact tangent	Approximate tangent	Exact tangent
1	3	3	3	3
2	3	3	3	3
3	3	3	4	4
4	4	4	4	4
5	4	4	5	5
6	5	5	5	5
7	5	>10	6	7
8	6	>10	7	div.
9	7	div.	8	–
10	7	–	9	–